Two-Phase Interleaved Boost PFC Converter With Coupled Inductor Under Single-Phase Operation

Fei Yang, *Member, IEEE*, Chunhui Li, Yong Cao, and Kai Yao, *Member, IEEE*

***Abstract*—When the interleaved boost power-factor correction (PFC) converter operates in a light load (<15% of nominal load), the phase-shedding control is commonly used to increase the converter's efficiency. If the inductors are coupled for high power density applications, because of the strong mutual effects of the coupled inductor, the switching of the operation phase may lead to a current flowing in the non-operation phase. In this paper, a two-phase interleaved boost PFC converter with a coupled inductor in the single-phase operation was analyzed. The operation modes of the converter in a switching cycle and a half line cycle were presented, and the modes' variation with the load changes, as well as the power distribution, was provided. A 1-kW prototype was built to verify the analysis, and it was shown that the non-operation phase also delivers some power, which may worsen the converter's efficiency and distort the average input current waveform.**

***Index Terms*—Coupled inductor, interleaved boost converter, power factor correction, single-phase operation.**

I. Introduction

THE boost converter is widely used in power-factor correction (PFC) applications for its high power factor (PF) and small input current ripple [1], and the interleaving technology is applied in power applications >600 W, which also increase the equivalent switching frequency and reduce the input and output current ripple [2], [3]. Furthermore, for requirements of high power density and high efficiency, the coupled inductor is usually used to reduce the volume of the magnetic components and the inductor current ripple, such as in the fields of electrical vehicles and fuel cell vehicles [4]–[8], renewable energy [9], [10], and interleaved boost dc–dc/PFC converter [11]–[20].

Normally, the design of the interleaved boost PFC converter is based on the rated power. However, the converter does not always work in a heavy load (80%–120% of nominal load), and the light load efficiency has drawn significant attention in recent years. Since the interleaving technology normally features relatively low efficiency in a light load, the phase-shedding control, managing the number of active phases, is a common method to optimize the system efficiency [21]–[25]. Zumel *et al*. [21] validates the phase-shedding control scheme in a multiphase converter and quantify the output voltage ripple to achieve a tradeoff between the efficiency improvement and output voltage capacitor. Qiu *et al*. [22] analyzes the power loss in multiphase voltage regulators with a phase-shedding control and define the optimal phase number under different load conditions. Su *et al*. [23] applies the phase-shedding control scheme in a multiphase interleaved dc–dc converter and estimate the load switching point from the lookup table of the power loss. Chen *et al*. [25] analyzes the transient behavior issues of an interleaved CCM boost PFC converter with the phase-shedding control and propose a new method to overcome load transient instability issues. Generally, the phase-shedding control can be freely used when the inductors are discrete, and the phase switching point can be estimated according to the operation modes and the converter efficiency.However, when the inductors are coupled, the coupling effects between the phases may make the converter operate in special operation modes. Imaoka *et al*. [26] proposes a magnetic design method for a multiphase interleaved boost dc–dc converter with a coupled inductor under a single-phase operation to solve the magnetic saturation problem, and the circulating current through a parallel diode of MOSFET in the no-driving phase is indicated. Barry *et al*. [27] analyzes the interleaved boost dc–dc converter with a coupled inductor in CCM and DCM, comprehensively, and present the force conduction phenomena of the reverse-paralleled diode of MOSFET and power diode. Yang *et al*. [28] classifies the coupling effects on the two-phase interleaved boost dc–dc converter in three circuit statuses and analyze the discontinuous operation modes in detail. The coupling effects may forward-bias the power diode or reverse-paralleled diode of MOSFET under some conditions, and they may change the two winding current waveforms, which is different from the non-coupled case. Most past literatures perform the analysis with a multiphase operation in a heavy load. For the light load condition with single-phase operation, however, the converter operation modes, relating with the coupling effects, and load and input voltage variation, are rarely analyzed. Therefore, the validity of the phase-shedding control and the rational utilization of the phase-shedding control are not clear.

In this paper, the operation modes of the two-phase interleaved boost PFC converter with a coupled inductor under a single-phase operation were analyzed. The coupling effects on the circuit were presented in Section II. The inductor current waveforms of each operation mode in a switching cycle were

Manuscript received February 28, 2019; accepted April 25, 2019. Date of publication May 5, 2019; date of current version October 18, 2019. This work was supported in part by the National Natural Science Foundation of China, China, under Grant 51707095, in part by the Natural Science Foundation of Jiangsu Province, China, under Grant BK20160837, and in part by the Fundamental Research Funds for the Central Universities, China, under Grant 30917011333. Recommended for publication by Associate Editor G. Moschopoulos. *(Corresponding author: Fei Yang.)*

The authors are with the School of Automation, Nanjing University of Science and Technology, Nanjing 210094, China (e-mail: yangfei@njust.edu.cn; 494668357@qq.com; 1778945313@qq.com; yaokai@njust.edu.cn).

Color versions of one or more of the figures in this paper are available online at http://ieeexplore.ieee.org.

Digital Object Identifier 10.1109/TPEL.2019.2914532

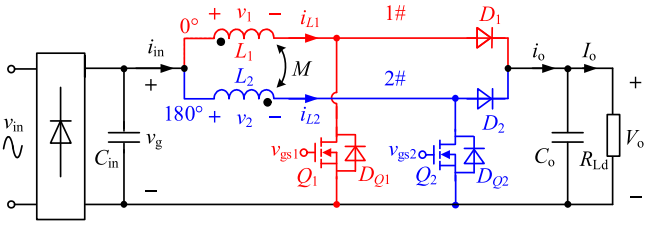

Fig. 1. Two-phase interleaved boost PFC converter with a coupled inductor.

analyzed, and their boundary duty cycles were calculated in Section III. On the basis of the analysis of the duty cycle of each operation mode, the operation modes in a half line cycle and their load-related variation rules, as well as the power distribution between the two phases, were obtained in Section IV, Finally, the experimental tests of a 1-kW prototype were presented in Section V.

II. Interleaved Boost PFC Converter Under a Single-Phase Operation

Fig. 1 depicts a two-phase interleaved boost PFC converter with an inversely coupled inductor. $v_{\rm in}$ is the input voltage, v_g the rectified input voltage, V_o the output voltage, and v_1 and v_2 the voltages, respectively, applied on Windings 1 and 2. D_1 and D_2 are power diodes, and Q_1 and Q_2 power switches. L_1 and L_2 are the self-inductances of the two windings and M their mutual inductance. Assuming that the two windings of the coupled inductor are identical, i.e., $L_1 = L_2 = L_{cp}$, the coupling coefficient $\alpha = M/L_{cp}$.

When the phase-shedding strategy is used on a two-phase interleaved converter, there is only one operation-phase. The switch status of the operation phase will affect the non-operation phase due to the coupling effect, which may make the currents flow in the two windings together [28], [29]. Taking Phase 1 as the operation-phase, we have the following:

1) When Q_1 is turned ON, the voltage of Winding 1, $v_1 = v_g$, and the voltage of Winding 2, $v_2 = -\alpha v_g$. The voltage applied on the drain-source of Q_2, $v_{\rm ds\_Q2} = v_g - v_2 = (1+\alpha)v_g$, and the reverse-paralleled diode D_{Q2} is reverse-biased since $v_{\rm ds\_Q2} > 0$. The voltage applied on D_2, $v_{D2} = v_g - v_2 - V_o = (1+\alpha)v_g - V_o$. If $v_g > V_o/(1+\alpha)$, $v_{D2} > 0$ and D_2 will be forward-biased, as shown in Fig. 2(a). Otherwise, Winding 2's current keeps 0.
2) When Q_1 is turned OFF, $v_1 = v_g - V_o$, $v_2 = -\alpha(v_g - V_o)$, and $v_{\rm ds\_Q2} = v_g - v_2 = (1+\alpha)v_g - \alpha V_o$. If $v_g < \alpha V_o(1+\alpha)$, $v_{\rm ds\_Q2} < 0$ and D_{Q2} will be forward-biased, as shown in Fig. 2(b). Otherwise, Winding 2's current keeps 0. $v_{D2} = v_g - v_2 - V_o = (1+\alpha)(v_g - V_o)$, and D_2 is reverse-biased since $v_{D2} < 0$.

Table I summarizes the coupling effects on the circuit statuses in three different ranges of input voltage [29].

From Fig. 1, the voltages of the two inductor windings can be expressed as

$$\begin{cases} v_1 = L_1 \cdot (di_{L1}/dt) - M \cdot (di_{L2}/dt) \\ v_2 = L_2 \cdot (di_{L2}/dt) - M \cdot (di_{L1}/dt). \end{cases} \tag{1}$$

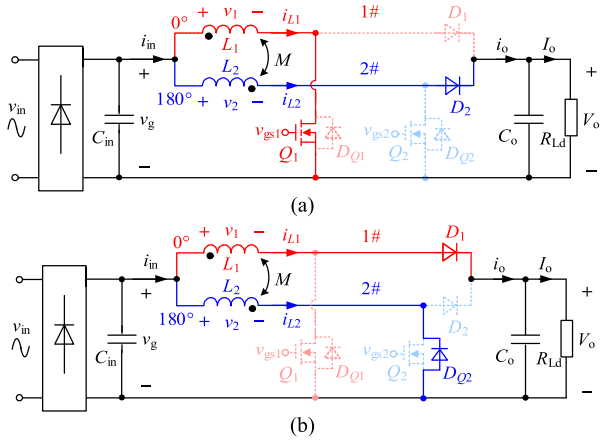

Fig. 2. Coupling effects on converter operations: (a) when $v_g > V_o/(1+\alpha)$, turn-ON of Q_1 makes the conduction of D_2, and (b) when $v_g < \alpha V_o(1+\alpha)$, turn-OFF of Q_1 makes the conduction of D_{Q2}.

TABLE I
Coupling Effects on Circuit Statuses

	$v_g < \alpha V_o/(1+\alpha)$	$\alpha V_o/(1+\alpha) \le v_g \le V_o/(1+\alpha)$	$v_g > V_o/(1+\alpha)$
Q_1 on	D_2 doesn't conduct	D_2 doesn't conduct	D_2 conducts
Q_1 off	D_{Q2} conducts	D_{Q2} doesn't conduct	D_{Q2} doesn't conduct

From (1), the following equation can be derived:

$$v_1 + \alpha \cdot v_2 = (1-\alpha^2) \cdot L_{cp} \cdot (di_{L1}/dt) \tag{2}$$

and the equivalent inductance $L_{\rm eq}$ is defined as

$$v_j = L_{\rm eq} \cdot (di_{Lj}/dt)\ (j = 1, 2)\,. \tag{3}$$

On the basis of the analysis above, the two-phase interleaved boost PFC converter with a coupled inductor under a single-phase operation has the following four operating states:

1) Q_1 is ON and D_2 is forward-biased ($v_1 = v_g$, $v_2 = v_g - V_o$);
2) Q_1 is ON and D_{Q2} is forward-biased, or Q_1 is OFF and D_2 is forward-biased ($v_1 = v_2 = v_g$ or $v_1 = v_2 = v_g - V_o$);
3) Q_1 is OFF and D_{Q2} is forward-biased ($v_1 = v_g - V_o$, $v_2 = v_g$);
4) one winding current or two winding currents keep 0.

When v_1, v_2 and their relationship are given, the corresponding $L_{\rm eq}$ for the two windings can be derived and presented in Table II [28], [29].

III. Operation Modes in a Switching Cycle

A. Operation Modes

On the basis of on Table I, the converter operation modes in a switching cycle under a single-phase operation can be clarified into three input voltage ranges as follows.

1) $v_g < \alpha V_o/(1+\alpha)$: Under this condition, when Q_1 turns ON, i_{L1} increases gradually with the equivalent inductance L_{cp}, and i_{L2} keeps 0. When Q_1 turns OFF, D_{Q2} is forward-biased, $v_1 = v_g - V_o$ and $v_2 = v_g$. The equivalent inductance of Winding 1, $L_{\rm eq3} > 0$, and the equivalent inductance of Winding 2,

TABLE II
EQUIVALENT INDUCTANCES OF TWO WINDINGS (Q_2 KEEPS OFF)

	Q_1 is on and D_2 is forward-biased (v_1=v_g, and v_2=v_g−V_o)	Q_1 is on and D_{Q2} is forward-biased, or Q_1 is off and D_2 is forward-biased (v_1=v_2=v_g, or v_1=v_2=v_g−V_o)	Q_1 is off and D_{Q2} is forward-biased (v_1=v_g−V_o, and v_2=v_g)	di_{L1}/dt=0 (i_{L1}=0) or di_{L2}/dt=0 (i_{L2}=0)
Winding 1	$L_{eq1}=\frac{(v_g/V_o)(1-\alpha^2)}{(1+\alpha)(v_g/V_o)-\alpha}L_{cp}$	$L_{eq2}=(1-\alpha)L_{cp}$	$L_{eq3}=\frac{(1-v_g/V_o)(1-\alpha^2)}{1-(1+\alpha)(v_g/V_o)}L_{cp}$	L_{cp}
Winding 2	$L_{eq3}=\frac{(1-v_g/V_o)(1-\alpha^2)}{1-(1+\alpha)(v_g/V_o)}L_{cp}$	$L_{eq2}=(1-\alpha)L_{cp}$	$L_{eq1}=\frac{(v_g/V_o)(1-\alpha^2)}{(1+\alpha)(v_g/V_o)-\alpha}L_{cp}$	L_{cp}

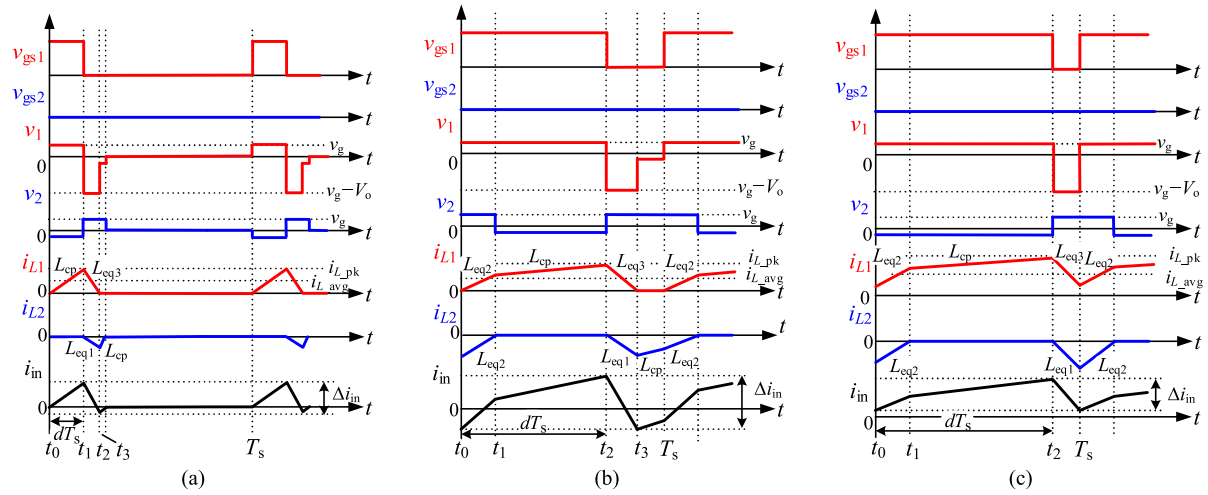

Fig. 3. Waveforms of (a) Mode 1a, (b) Mode 1b, and (c) Mode 1c in a switching cycle when $v_g < \alpha V_o/(1+\alpha)$.

$L_{eq1} < 0$. Therefore, i_{L1} decreases from the peak current, while i_{L2} increases from 0 in the negative direction. When i_{L1} reaches 0, $v_2 = v_g$ and $v_1 = -\alpha v_g$. Then, the equivalent inductance of Winding 2, $L_{cp} > 0$, and i_{L2} decreases from the negative peak current and reaches 0 before the next switching cycle. This is defined as Mode 1a, as shown in Fig. 3(a).

If the duty cycle is increased, i_{L2} will not reach 0 before the next switching cycle. When Q_1 turns ON at the next switching cycle, $v_1 = v_g$ and $v_2 = v_g$. Both the equivalent inductances of the two windings, L_{eq2}>0, and i_{L2} decrease to 0 with a slope of v_g/L_{eq2}, while i_{L1} increases from 0 with a slope of v_g/L_{eq2}. This is defined as Mode 1b, as shown in Fig. 3(b).

If i_{L1} does not reach 0 before the next switching cycle and remains continuous, under this condition when Q_1 turns ON at the next switching cycle, $v_1 = v_g$ and $v_2 = v_g$. The equivalent inductance of the two windings is L_{eq2}, and i_{L1} and i_{L2} increase with the slope of v_g/L_{eq2}. This is defined as Mode 1c, as shown in Fig. 3(c).

2) $\alpha V_o/(1+\alpha) \le v_g \le V_o/(1+\alpha)$*:* Under this condition, the coupling effects cannot lead to the conduction of D_2 or D_{Q2}, and i_{L2} always keeps 0. For a short duty cycle case, i_{L1} increases when Q_1 turns ON and decreases when Q_1 turns OFF. Then, i_{L1} remains 0 till the next switching cycle, as shown in Fig. 4(a), which is defined as Mode 2a. If the duty cycle increases, i_{L1} will be continuous, as shown in Fig. 4(b), and the converter operates in Mode 2b.

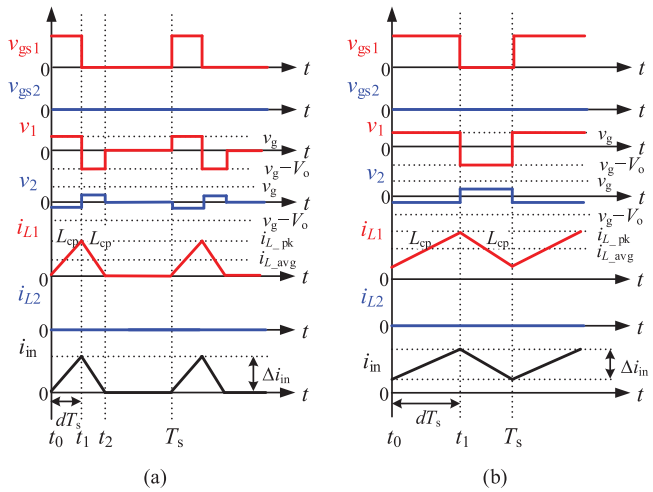

Fig. 4. Waveforms of (a) Mode 2a and (b) Mode 2b in a switching cycle when $\alpha V_o/(1+\alpha) \le v_g \le V_o/(1+\alpha)$.

3) $v_g > V_o/(1+\alpha)$*:* The converter has two operation modes under this condition. When Q_1 turns ON, due to the force conduction of D_2, $v_1 = v_g$ and $v_2 = v_g - V_o$. The equivalent inductance of Winding 1, L_{eq1}>0, and the equivalent inductance of Winding 2, L_{eq3}<0. Therefore, i_{L1} increases from 0 with a slope of v_g/L_{eq1}, while i_{L2} also increases from 0 with

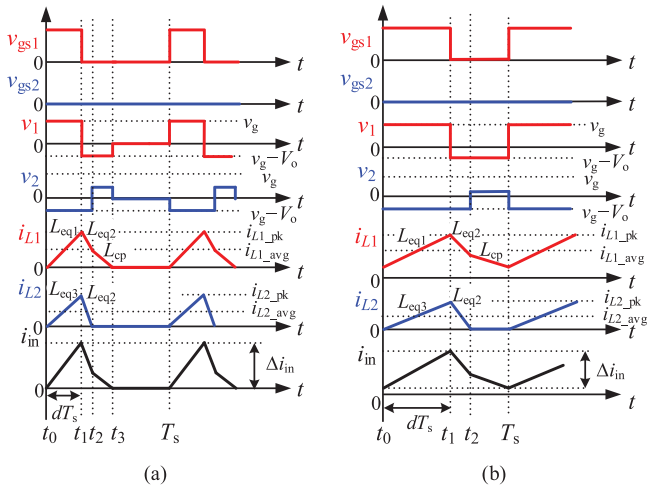

Fig. 5. Waveforms of (a) Mode 3a and (b) Mode 3b in a switching cycle when $v_g > V_o/(1+\alpha)$.

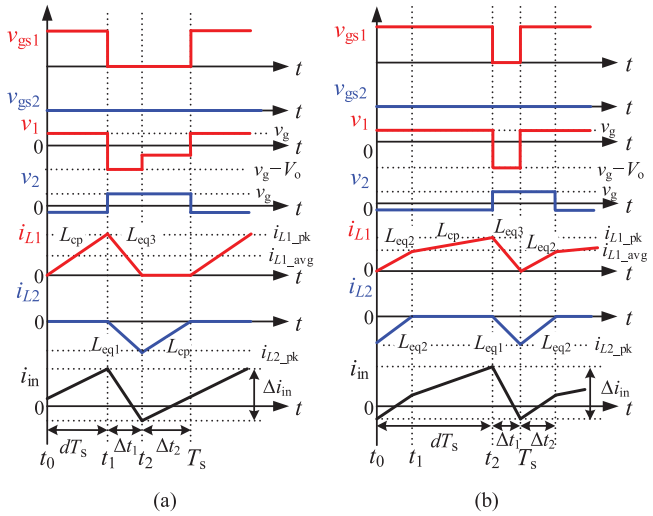

Fig. 6. Critical modes (a) between Mode 1a and 1b, and (b) between Mode 1b and 1c, when $v_g < \alpha V_o/(1+\alpha)$.

a slope of $(v_g - V_o)/L_{eq3}$. When Q_1 turns OFF, $v_1 = v_g - V_o$ and $v_2 = v_g - V_o$. Both i_{L1} and i_{L2} decrease from their peak currents with the equivalent inductance L_{eq2}>0. Since the peak value of i_{L2} is less than i_{L1}, i_{L2} reaches 0 before i_{L1}. When i_{L2} reaches 0, $v_1 = v_g - V_o$ and $v_2 = \alpha(V_o - v_g)$. Then, i_{L1} decreases to 0 with a slope of $(V_o - v_g)/L_{cp}$, while i_{L2} remains 0. This operation mode, as shown in Fig. 5(a), is defined as Mode 3a. If the duty cycle is increased, i_{L1} will not reach 0 before the next switching cycle and will be continuous, as shown in Fig. 5(b), and this is defined as Mode 3b.

B. Boundary Duty Cycle

The operation modes in a switching cycle are characterized by the duty cycle, and the boundary duty cycle of the operation modes are analyzed in detail as follows.

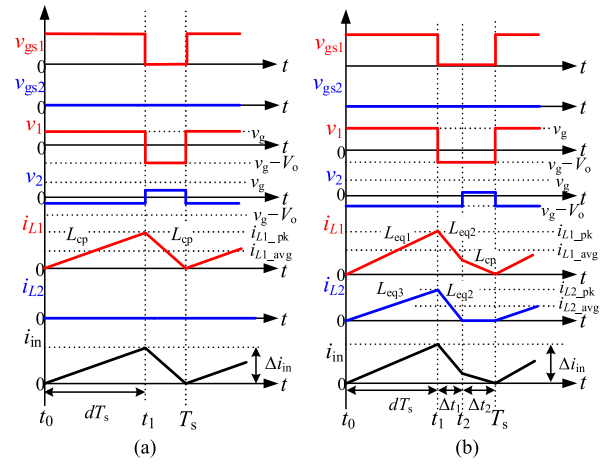

Fig. 7. Critical mode between (a) Mode 2a and 2b when $\alpha V_o/(1+\alpha) \le v_g \le V_o/(1+\alpha)$, and (b) between Mode 3a and 3b when $v_g > V_o/(1+\alpha)$.

1) $v_g < \alpha V_o/(1+\alpha)$*:* Fig. 6(a) shows the waveforms of the critical mode between Modes 1a and 1b, from which we can obtain

$$\begin{cases} dT_s \cdot (v_g/L_{cp}) = \Delta t_1 \cdot (V_o - v_g)/L_{\text{eq3}} \\ \Delta t_1 \cdot v_g/(-L_{\text{eq1}}) = \Delta t_2 \cdot v_g/L_{cp} \\ dT_s + \Delta t_1 + \Delta t_2 = T_s. \end{cases} \tag{4}$$

Since Q_1 turns ON in the next switching cycle, when i_{L2} reaches 0, the boundary duty cycle of Modes 1a and 1b can be derived from (4) as

$$d = 1/(1+\alpha). \tag{5}$$

Fig. 6(b) shows the waveforms of the critical mode between Modes 1b and 1c. Q_1 turns ON in the next switching cycle when i_{L1} decrease to 0. Then, we obtain

$$\begin{cases} (-v_g/L_{\text{eq1}})\,\Delta t_1 = (v_g/L_{\text{eq2}})\,\Delta t_2 \\ (v_g/L_{\text{eq2}})\,\Delta t_2 + (v_g/L_{cp}) \\ (dT_s - \Delta t_2) = [(V_o - v_g)/L_{\text{eq3}}]\,\Delta t_1 \\ dT_s + \Delta t_1 = T_s \end{cases} \tag{6}$$

and the boundary duty cycle of Modes 1b and 1c is

$$d = (V_o - v_g)/V_o. \tag{7}$$

Therefore, for $v_g < \alpha V_o/(1+\alpha)$, when $d < 1/(1+\alpha)$, $1/(1+\alpha) < d < (V_o - v_g)/V_o$, and $d = (V_o - v_g)/V_o$, the converter works in Modes 1a, 1b, and 1c, respectively.

2) $\alpha V_o/(1+\alpha) \le v_g \le V_o/(1+\alpha)$*:* Fig. 7(a) shows the critical mode between Modes 2a and 2b. Q_1 turns ON in the next switching cycle when i_{L1} reaches 0. We obtain

$$(v_g/L_{cp})\,dT_s = [(V_o - v_g)/L_{cp}]\,(T_s - dT_s) \tag{8}$$

and the boundary duty cycle of Modes 2a and 2b is

$$d = (V_o - v_g)/V_o. \tag{9}$$

Therefore, for $\alpha V_o/(1+\alpha) \le v_g \le V_o/(1+\alpha)$, when $d < (V_o - v_g)/V_o$ and $d = (V_o - v_g)/V_o$, the converter works in Modes 2a and 2b, respectively.

TABLE III
DISTRIBUTION OF OPERATION MODES

	$v_g<\alpha V_o/(1+\alpha)$	$\alpha V_o/(1+\alpha)\le v_g \le V_o/(1+\alpha)$	$v_g>V_o/(1+\alpha)$
$0<d<1/(1+\alpha)$	Mode 1a	Mode 2a	Mode 3a
$1/(1+\alpha)\le d\le(V_o-v_g)/V_o$	Mode 1b		
$d=(V_o-v_g)/V_o$	Mode 1c	Mode 2b	Mode 3b

3) $v_g > V_o/(1+\alpha)$*:* Fig. 7(b) shows the waveforms of the critical mode between Modes 3a and 3b. Since Q_1 turns ON in the next switching cycle when i_{L1} decreases to 0, we can obtain

$$\begin{cases} \left[(v_g - V_o)/L_{\text{eq3}}\right] dT_s = \left[(V_o - v_g)/L_{\text{eq2}}\right] \Delta t_1 \\ (v_g/L_{\text{eq1}})\, dT_s = \left[(V_o - v_g)/L_{\text{eq2}}\right] \\ \Delta t_1 + \left[(V_o - v_g)/L_{cp}\right] \Delta t_2 \\ dT_s + \Delta t_1 + \Delta t_2 = T_s \end{cases} \tag{10}$$

and the boundary duty cycle of Modes 3a and 3b is

$$d = (V_o - v_g)/V_o. \tag{11}$$

Therefore, for $v_g > V_o/(1+\alpha)$, when $d < (V_o - v_g)/V_o$ and $d = (V_o - v_g)/V_o$, the converter works in Modes 3a and 3b, respectively.

Table III summarizes the distribution of the operation modes and their boundary duty cycles.

IV. Operation Modes in a Half Line Cycle

A. Duty Cycle of Average Current Control

From Table III, the operation modes in a half line cycle are determined by the input voltage, v_g, and duty cycle d.

Normally, the rectified input voltage, v_g, is

$$v_g = \sqrt{2} V_{\text{in}} \left|\sin(\omega t)\right| \tag{12}$$

where $\omega = 2\pi f_{\text{line}}$ is the angular frequency and f_{line} the line voltage frequency. The average inductor current of the operation phase can be expressed as

$$i_{L1\_\text{avg}} = \sqrt{2}\,(P_{1L}/V_{\text{in}})\left|\sin\omega t\right| = P_{1L} v_g / V_{\text{in}}^2 \tag{13}$$

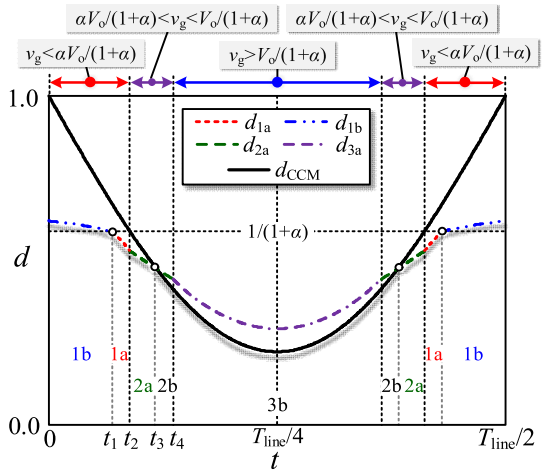

Fig. 8. Duty cycle of each mode in a half line cycle.

where P_{1L} is the input power of the operation phase.

For unity PF, the duty cycle of the operation phase is normally calculated on the basis of the average winding current in sinusoid. When the inductor current is continuous, such as in Modes 1c, 2b, and 3b, the duty cycle, meeting the voltage-second balance, can be expressed as

$$d_{\text{CCM}} = (V_o - v_g)/V_o. \tag{14}$$

When the inductor current is discontinuous, such as in Modes 1a, 1b, 2a, and 3a, the average inductor current in a switching period $(t_0 \sim T_s)$ of these operation modes can be derived from Figs. 3(a)–4(a), and 5(a) as (15) shown at the bottom of this page. Substituting (13) into (15), the duty cycle each of these modes can be derived as (16), shown at the bottom of this page.

B. Operation Modes Variation With Load

When the specific parameters of the converter are given, the duty cycle in a half line cycle, as well as the operation modes, can be figured out from (14) and (16). Fig. 8 presents an example of the duty cycle in a half line cycle. It should be noted

$$\begin{cases} i_{L1\_\text{avg}\_1a} = v_g\left[\alpha(1+\alpha)v_g - V_o\right]\cdot d^2 / \left\{2L_{cp}f_s\left[(1+\alpha)v_g - V_o\right]\right\} & \text{Mode 1a} \\ i_{L1\_\text{avg}\_1b} = v_g\left\{(1+\alpha)^2 V_o \cdot d^2 - 2\alpha(1+\alpha)^2 v_g \cdot d + \alpha\left[(1+\alpha)^2 v_g - V_o\right]\right\} / \\ \left\{2L_{cp}f_s(1-\alpha^2)(1+\alpha)\left[V_o - (1+\alpha)v_g\right]\right\} & \text{Mode 1b} \\ i_{L1\_\text{avg}\_2a} = V_o v_g \cdot d^2 / \left[2f_s L_{cp}(V_o - v_g)\right] & \text{Mode 2a} \\ i_{L1\_\text{avg}\_3a} = V_o\left[(1+\alpha)v_g - \alpha^2 V_o\right]\cdot d^2 / \left[2f_s L_{cp}(V_o - v_g)(1-\alpha)(1+\alpha)^2\right] & \text{Mode 3a} \end{cases} \tag{15}$$

$$\begin{cases} d_{1a} = \sqrt{2f_s L_{cp} P_{1L}\left[V_o - (1+\alpha)v_g\right] / \left\{V_{\text{in}}^2\left[V_o - \alpha(1+\alpha)v_g\right]\right\}} \\ d_{1b} = \alpha v_g / V_o + \sqrt{\left[V_o - (1+\alpha)v_g\right]\cdot\left\{\alpha V_{\text{in}}^2\left[V_o - \alpha(1+\alpha)v_g\right] + 2L_{cp}f_s P_{1L} V_o(1-\alpha^2)(1+\alpha)\right\}} / \left[V_o V_{\text{in}}(\alpha+1)\right] \\ d_{2a} = \sqrt{2f_s L_{cp} P_{1L}(V_o - v_g)/\left(V_{\text{in}}^2 V_o\right)} \\ d_{3a} = \sqrt{2f_s L_{cp} P_{1L}\left[v_g(V_o - v_g)(1-\alpha)(1+\alpha)^2\right] / \left\{V_{\text{in}}^2 V_o\left[(1+\alpha)v_g - \alpha^2 V_o\right]\right\}} \end{cases} \tag{16}$$

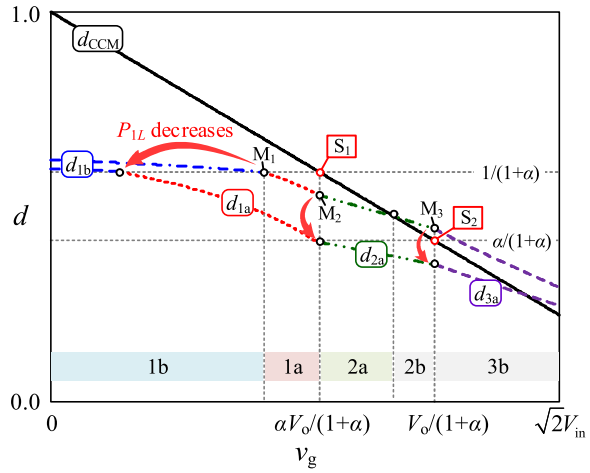

Fig. 9. Variation of points M_1, M_2, and M_3 as P_{1L} changes.

that if a shorter duty cycle meets the requirement of the average current control, the converter would not operate with a longer duty cycle. Therefore, although there are more than one duty cycle value meet the average current requirements under a specific time point, the duty cycle is the smallest one. As a result, the operating duty cycle is the minimum value envelope of those calculated duty cycles. Since the variation of the operation modes in a half line is symmetrical, the analysis of the modes variation is performed in [0, T_{line}/4]. When $v_g < \alpha V_o/(1+\alpha)$, since the minimum duty cycle is d_{1b} in [0, t_1] and d_{1a} in [t_1, t_2], the converter operates in Modes 1b and 1a, respectively. When $\alpha V_o/(1+\alpha) \le v_g \le V_o/(1+\alpha)$, the minimum duty cycle is d_{2a} in [t_2, t_3] and d_{CCM} in [t_3, t_4], so the converter operates in Modes 2a and 2b, respectively. When $v_g > V_o/(1+\alpha)$, the minimum duty cycle is d_{CCM}, so the converter operates in Mode 3b in [t_4, T_{line}/4].

As the load changes, the operation modes in a half line cycle also change because of the duty cycle variation. Since the duty cycles are related with v_g from (14) and (16), the analysis of the operation mode variation in a half line cycle as the load change can be turned into the analysis of the relationship between the minimum duty cycle and v_g in $[0, \sqrt{2}V_{\text{in}}]$.

From (14) and (16), Fig. 9 shows the duty cycle of each mode varying with v_g in $[0, \sqrt{2}V_{\text{in}}]$, corresponding to Fig. 8, and there are some boundary points between the operation modes. The curve of d_{CCM} intersects with the line $v_g = \alpha V_o/(1+\alpha)$ and $v_g = V_o/(1+\alpha)$ at points of S_1 $(\alpha V_o/(1+\alpha),\ 1/(1+\alpha))$ and S_2 $(V_o/(1+\alpha),\ \alpha/(1+\alpha))$, respectively, which are independent of P_{1L}. The intersection points of curves d_{1a} and d_{1b}, d_{1a} and d_{2a}, and d_{2a} and d_{3a} are defined as M_1, M_2, and M_3, respectively, which have a relationship with P_{1L}. As P_{1L} decreases, all the duty cycles decrease generally; M_1 moves to left along the line of $d = 1/(1+\alpha)$; M_2 and M_3 move down along the line of $v_g = \alpha V_o/(1+\alpha)$ and line of $v_g = V_o/(1+\alpha)$, respectively.

As V_{in} changes, the range of v_g, $[0, \sqrt{2}V_{\text{in}}]$, changes in a half line cycle, as well as the operation modes. When $\sqrt{2}V_{\text{in}} < \alpha V_o/(1+\alpha)$, $v_g < \alpha V_o/(1+\alpha)$ and the operation modes, occurred in a half line cycle, are just Modes 1a, 1b, and 1c. When $\alpha V_o/(1+\alpha) < \sqrt{2}V_{\text{in}} < V_o/(1+\alpha)$, Modes 2a and 2b will occur. When $\sqrt{2}V_{\text{in}} > V_o/(1+\alpha)$, all the operation modes may occur in a half line cycle. The variation of the operation modes with the load change is analyzed in detail as follows.

1) $\sqrt{2}V_{\text{in}} < \alpha V_o/(1+\alpha)$*:* There are four boundary powers in this voltage range, and only Modes 1a, 1b, or 1c occurs. As P_{1L} increases from the light load to the heavy load, M_1 moves along the line of $d = 1/(1+\alpha)$ from (0, $1/(1+\alpha)$) to S_1. When M_1 moves to (0, $1/(1+\alpha)$), as shown in Fig. 10(a), the first boundary power P_{11} is derived from (16) by the substitution of $v_g = 0$ into $d_{1a} = 1/(1+\alpha)$ as

$$P_{11} = V_{\text{in}}^2 / \left[2L_{cp}f_s(1+\alpha)^2\right]. \tag{17}$$

Therefore, when $0 < P_{1L} < P_{11}$, only Mode 1a occurs in a half line cycle since the minimum duty cycle is d_{1a}.

As the load increases, when $P_{1L} > P_{11}$, Mode 1b appears. When M_1 moves to $(\sqrt{2}V_{\text{in}}, 1/(1+\alpha))$, as shown in Fig. 10(b), the second boundary power P_{12} is derived from (16) by the substitution of $v_g = \sqrt{2}V_{\text{in}}$ into $d_{1a} = 1/(1+\alpha)$ as

$$P_{12} = \frac{V_{\text{in}}^2\left[V_o - \sqrt{2}V_{\text{in}}\alpha(1+\alpha)\right]}{2L_{cp}f_s(1+\alpha)^2\left[V_o - \sqrt{2}V_{\text{in}}(1+\alpha)\right]}. \tag{18}$$

When $P_{11} < P_{1L} < P_{12}$, Modes 1b and 1a occur successively.

As the load further increases, when M_1 moves to the right of $(\sqrt{2}V_{\text{in}}, 1/(1+\alpha))$, and d_{1b} and d_{CCM} intersect at $v_g = \sqrt{2}V_{\text{in}}$, as shown in Fig. 10(c), then P_{13} can be obtained from (16) by the substitution of $v_g = \sqrt{2}V_{\text{in}}$ into $d_{\text{CCM}} = d_{1b}$ as

$$P_{13} = \frac{V_{\text{in}}^2 V_o(\alpha^2+\alpha+1) - \sqrt{2}V_{\text{in}}^3(2\alpha^2+3\alpha+1)}{2L_{cp}f_s V_o(1-\alpha)(1+\alpha)^2}. \tag{19}$$

When $P_{12} < P_{1L} < P_{13}$, only Mode 1b occurs since the minimum duty cycle is d_{1b}.

As the load increases, when $P_{1L} > P_{13}$, Mode 1c appears. When M_1 moves to the right continuously, and d_{1b} and d_{CCM} intersect at $v_g = 0$, as shown in Fig. 10(d), the last boundary power P_{14} can be derived from (16) by the substitution of $v_g = 0$ into $d_{\text{CCM}} = d_{1b}$ as

$$P_{14} = V_{\text{in}}^2\left(\alpha^2+\alpha+1\right) / \left[2L_{cp}f_s(1+\alpha)^2(1-\alpha)\right]. \tag{20}$$

When $P_{13} < P_{1L} < P_{14}$, Modes 1b and 1c occur since the minimum duty cycle is d_{1b} and d_{CCM} in succession, and the converter enters into partial CCM.

When $P_{1L} > P_{14}$, only Mode 1c occurs since the minimum duty cycle is d_{CCM}, and the converter operates in full CCM.

Fig. 11 shows the operation-mode-occurring condition as the load increases when $\sqrt{2}V_{\text{in}} < \alpha V_o/(1+\alpha)$.

2) $\alpha V_o/(1+\alpha) \le \sqrt{2}V_{\text{in}} \le V_o/(1+\alpha)$*:* There are also four boundary powers in this voltage range, and Modes 2a or 2b will occur in a half line cycle. With the increase of P_{1L}, M_1 moves right along $d = 1/(1+\alpha)$, while M_2 moves up along $v_g = \alpha V_o/(1+\alpha)$.

The first boundary power P_{21}, as M_1 moves to $v_g = 0$, is similar to P_{11}, as shown in Fig. 12(a). When $0 < P_{1L} < P_{21}$,

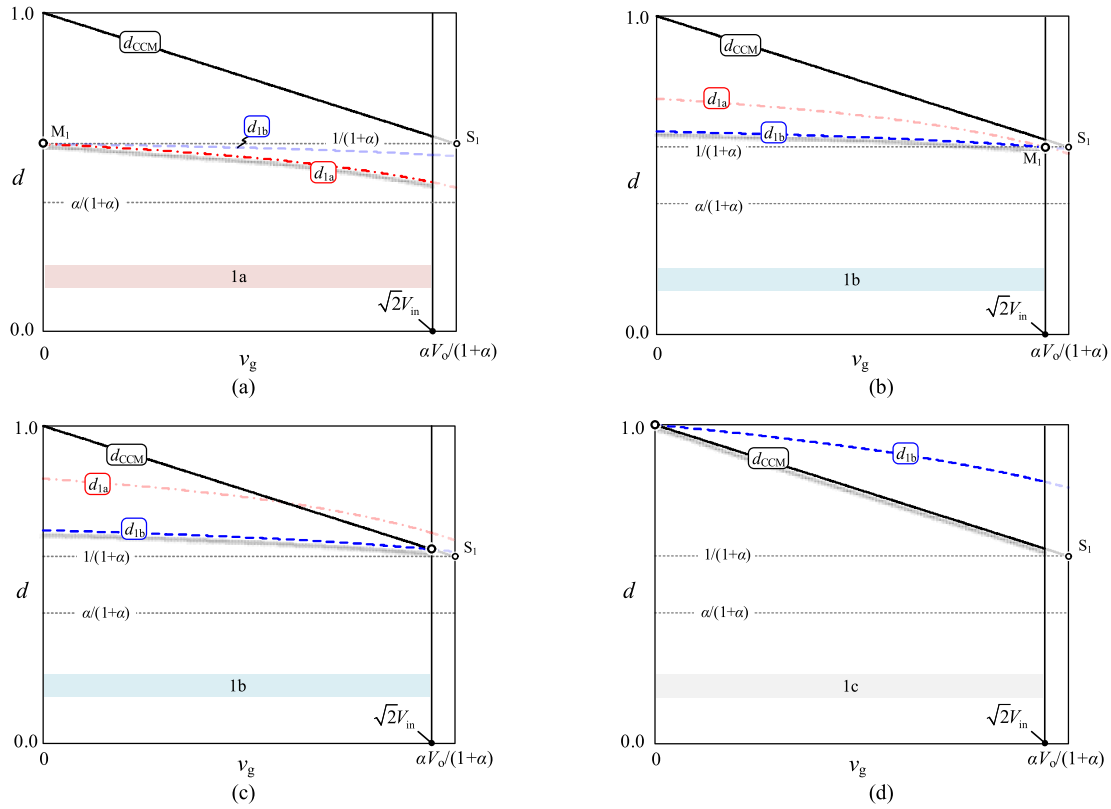

Fig. 10. Duty cycle at boundary powers (a) P_{11}, (b) P_{12}, (c) P_{13}, and (d) P_{14}, when $\sqrt{2}V_{\rm in} < \alpha V_o/(1+\alpha)$.

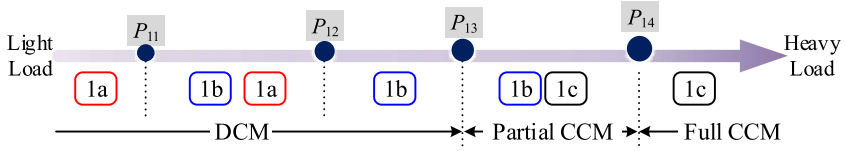

Fig. 11. Variation of modes in a half line cycle as the load changes when $\sqrt{2}V_{\rm in} < \alpha V_o/(1+\alpha)$.

since the minimum duty cycles are d_{1a} and d_{2a}, Modes 1a and 2a occur in a half line cycle

As the load increases, M_2 moves up, and d_{2a} and $d_{\rm CCM}$ will intersect at $v_g = \sqrt{2}V_{\rm in}$, as shown in Fig. 12(b). Substituting $v_g = \sqrt{2}V_{\rm in}$ into $d_{\rm CCM} = d_{2a}$, the second boundary power P_{22} can be derived from (16) as

$$P_{22} = V_{\rm in}^2(V_o - \sqrt{2}V_{\rm in})/\left(2L_{cp}f_sV_o\right). \tag{21}$$

When $P_{21} < P_{1L} < P_{22}$, Modes 1b, 1a, and 2a occur successively.

As the load increases, when M_1 and M_2 intersect at S_1, as shown in Fig. 12(c), the third boundary power P_{23} can be derived by substituting $v_g = \alpha V_o/(1+\alpha)$ into $d_{1a} = 1/(1+\alpha)$ as

$$P_{23} = V_{\rm in}^2/\left[2L_{cp}f_s(1+\alpha)\right]. \tag{22}$$

When $P_{22} < P_{1L} < P_{23}$, since the minimum duty cycles are d_{1b}, d_{1a}, d_{2a}, and $d_{\rm CCM}$, Modes 1b, 1a, 2a, and 2b occur, and the converter enters into partial CCM.

The last boundary power P_{24} is similar to P_{14}, which occurs when d_{1b} and $d_{\rm CCM}$ intersect at $v_g = 0$, as shown in Fig. 12(d). So, when $P_{23} < P_{1L} < P_{24}$, Modes 1b, 1c, and 2b occur, since the minimum duty cycles are d_{1b} and $d_{\rm CCM}$.

When $P_{1L} > P_{24}$, the minimum duty cycle is $d_{\rm CCM}$; Modes 1c and 2b occur, and the converter enters into full CCM.

Fig. 13 shows the operation-mode-occurring condition as the load increases when $\alpha V_o/(1+\alpha) < \sqrt{2}V_{\rm in} < V_o/(1+\alpha)$.

3) $\sqrt{2}V_{\rm in} > V_o/(1+\alpha)$*:* There are five boundary powers in this voltage range, and Modes 3a or 3b will occur. With the increase of P_{1L}, M_3 moves up along $v_g = V_o/(1+\alpha)$, while M_1 moves right along $d = 1/(1+\alpha)$ and M_2 moves up along $v_g = \alpha V_o/(1+\alpha)$.

When d_{3a} and $d_{\rm CCM}$ intersect at $v_g = \sqrt{2}V_{\rm in}$, as shown in Fig. 14(a), the first boundary power P_{31} can be derived from (16) by substituting $v_g = \sqrt{2}V_{\rm in}$ into $d_{3a} = d_{\rm CCM}$ as

$$P_{31} = \frac{\sqrt{2}V_{\rm in}\left(V_o - \sqrt{2}V_{\rm in}\right)\left[\sqrt{2}\left(1+\alpha\right)V_{\rm in} - \alpha^2V_o\right]}{4L_{cp}f_sV_o(1-\alpha)(1+\alpha)^2} \tag{23}$$

and when $0 < P_{1L} < P_{31}$, Modes 1a, 2a, and 3a occur since the minimum duty cycles are d_{1a}, d_{2a}, and d_{3a}.

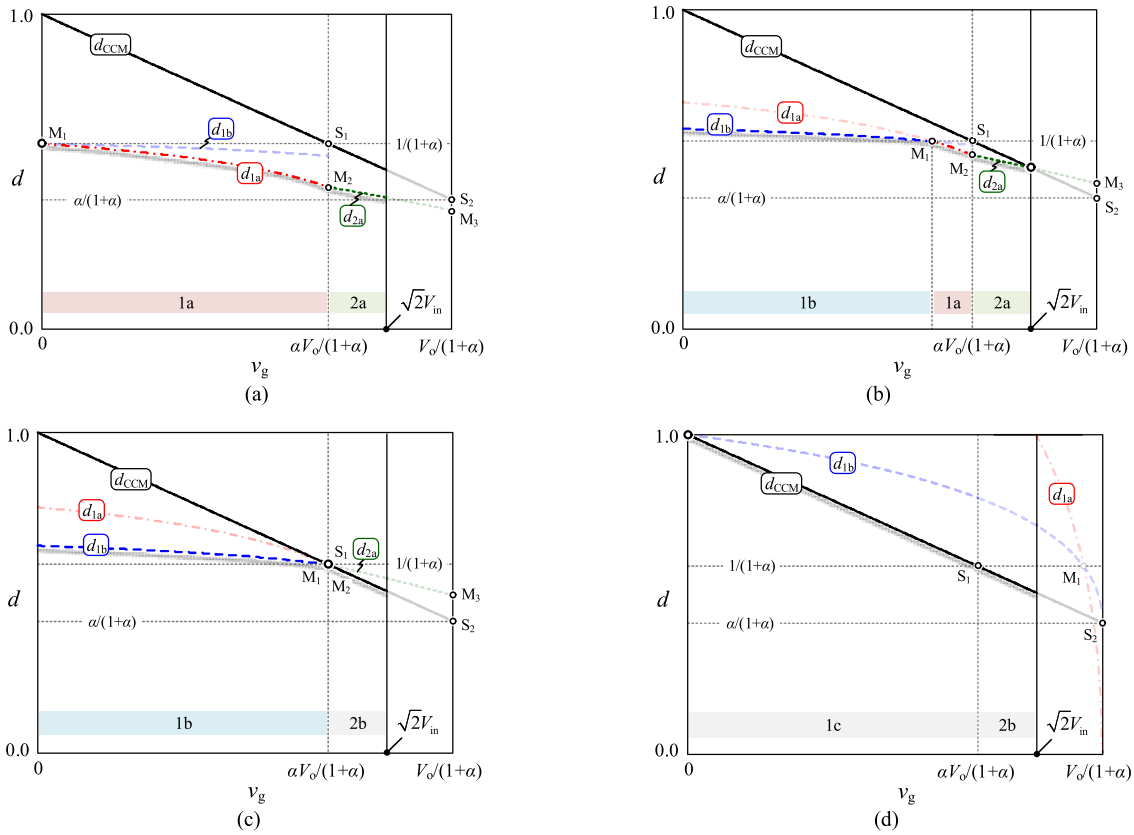

Fig. 12. Duty cycle at boundary powers (a) P_{21}, (b) P_{22}, (c) P_{23}, and (d) P_{24}, when $\alpha V_o/(1+\alpha) \le \sqrt{2}V_{\rm in} \le V_o/(1+\alpha)$.

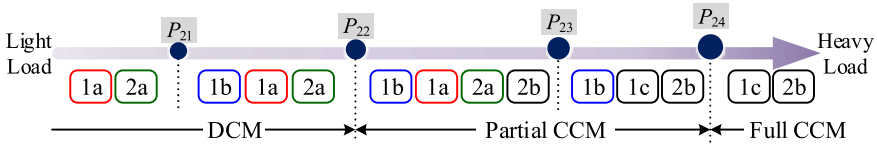

Fig. 13. Variation of modes in a half line cycle as the load changes when $\alpha V_o/(1+\alpha) \le \sqrt{2}V_{\rm in} \le V_o/(1+\alpha)$.

When M_1 moves to $v_g = 0$ as the load increases, as shown in Fig. 14(b), the second boundary power P_{32} is similar to P_{11} and P_{21}. When $P_{31} < P_{1L} < P_{32}$, Modes 1a, 2a, 3a, and 3b occur, since the minimum duty cycles are d_{1a}, d_{2a}, d_{3a}, and $d_{\rm CCM}$, and the converter enters into partial CCM.

As M_3 moves to S_2, as shown in Fig. 14(c), the third boundary power P_{33} can be obtained by substituting $v_g = V_o/(1+\alpha)$ into $d_{2a} = \alpha/(1+\alpha)$ as

$$P_{33} = \alpha V_{\rm in}^2 / \left[2L_{cp} f_s (1+\alpha)\right] \tag{24}$$

and when $P_{32} < P_{1L} < P_{33}$, Modes 1b, 1a, 2a, 3a, and 3b occur, successively.

When M_1 and M_2 intersect at S_1, as shown in Fig. 14(d), the fourth boundary power P_{34} is similar to P_{23}. When $P_{33} < P_{1L} < P_{34}$, Modes 1b, 1a, 2a, 2b, and 3b occur.

When d_{1b} and $d_{\rm CCM}$ intersect at $v_g = 0$, as shown in Fig. 14(e), the last boundary power P_{35} is similar to P_{14} and P_{24}, and when $P_{34} < P_{1L} < P_{35}$, Modes 1b, 1c, 2b, and 3b occur.

When $P_{1L} > P_{35}$, Modes 1c, 2b, and 3b occur, and the converter enters into full CCM.

Fig. 15 shows the operation-mode-occurring condition as the load increase when $\sqrt{2}V_{\rm in} > V_o/(1+\alpha)$.

C. Operation Modes in a Half Line Cycle

When the specific parameters of the converter are given, the boundary power is calculated from (17)–(24). For a specific input power of the operation phase, P_{1L}, the operating duty cycles in a half line cycle can be calculated from (12)–(16), and the whole operation mode map in a half line cycle is formed from Figs. 10–15. With a specific duty cycle and the converter parameters, the corresponding operation mode is confirmed from the boundary duty cycle expressions (4)–(11) and Table III. Then, on the basis of (1)–(3) and Table II, the inductor current

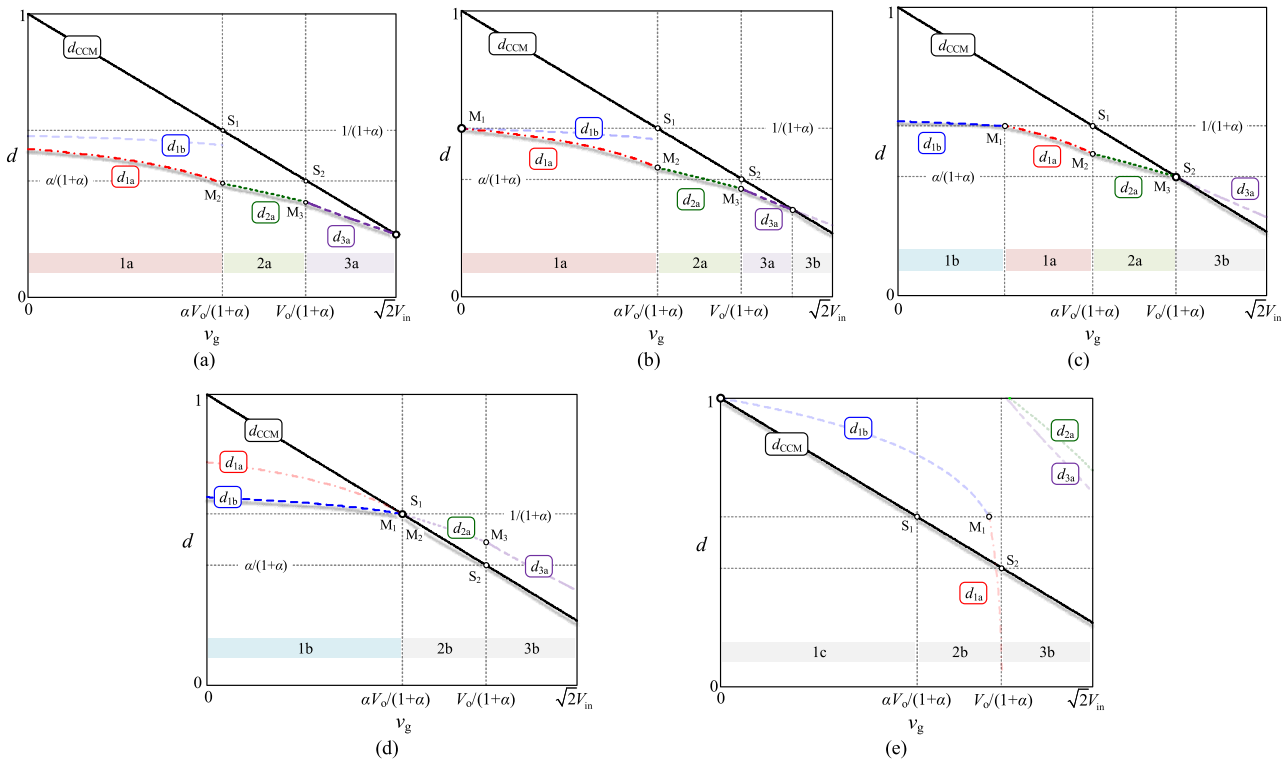

Fig. 14. Duty cycle at boundary powers (a) P_{31}, (b) P_{32}, (c) P_{33}, (d) P_{34}, and (e) P_{35}, when $\sqrt{2}V_{\rm in} > V_o/(1+\alpha)$.

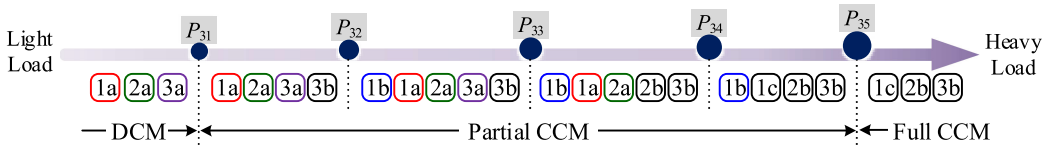

Fig. 15. Variation of modes in a half line cycle as the load changes when $\sqrt{2}V_{\rm in} > V_o/(1+\alpha)$.

expressions of the operation mode in each switching cycle can be obtained, and both the winding current waveforms can be depicted. At last, the average winding currents, input current, and power factor can be calculated.

If $V_o = 400$ V, $L_c p = 500\,\mu$H, and $\alpha = 0.7$, take $V_{\rm in} = 110$ V and $V_{\rm in} = 220$ V as examples to show the operation modes in a half line. For $V_{\rm in} = 110$ V, $\sqrt{2}V_{\rm in} < \alpha V_o/(1+\alpha)$, $P_{11} = 42$ W, $P_{12} = 66$ W, $P_{13} = 84$ W, and $P_{14} = 306$ W. Fig. 16 depicts the peak envelop of the inductor current in a half line cycle, as well as the operation modes, at $P_{1L} = 30$ W, $P_{1L} = 60$ W, and $P_{1L} = 100$ W, respectively. Since 30 W $< P_{11}$, $P_{11} < 60$ W $< P_{12}$, and $P_{13} < 100$ W $< P_{14}$, the operation modes in a half line cycle are Modes 1a, 1a, and 1b, and Modes 1b and 1c, respectively, which matches the analysis in Fig. 11.

For $V_{\rm in} = 220$ V, $\sqrt{2}V_{\rm in} > V_o/(1+\alpha)$, $P_{31} = 133$ W, $P_{32} = 167$ W, $P_{33} = 199$ W, $P_{34} = 285$ W, and $P_{35} = 1223$ W. Fig. 17 depicts the waveforms of inductor current and operation modes in a half line cycle at $P_{1L} = 100$ W, $P_{1L} = 200$ W, and $P_{1L} = 400$ W. Since 100 W $< P_{31}$, $P_{33} < 200$ W $< P_{34}$, and $P_{34} < 400$ W$< P_{35}$, the operation modes in a half line cycle are Modes 1a, 2a, and 3a, Modes 1b, 1a, 2a, 2b, and 3b, and Modes 1b, 1c, 2b, and 3b, respectively, which matches the analysis in Fig. 17.

On the basis of the analysis above, the converter operation modes in a half line cycle under any input voltage and load, as well as their winding current waveforms, can be obtained. This is helpful to predict the operation condition of the converter.

D. Power Distribution of Two Phases

From Figs. 16 and 17, the input power of operation phase P_{1L} flows from source to load, and a part of the input power P_{2L} would flow through the non-operation phase due to the conduction of D_2 or D_{Q2}: When $v_g < \alpha V_o/(1+\alpha)$, P_{2L} flows through D_{Q2} returning back to the source, as shown in Fig. 18(a); when $\alpha V_o/(1+\alpha) \le v_g \le V_o/(1+\alpha)$, P_{2L} is 0, as shown in Fig. 18(b); when $v_g > V_o/(1+\alpha)$, P_{2L} flows through D_2 to the load, as shown in Fig. 18(c). This may worsen the converter efficiency and distort the average input current waveform.

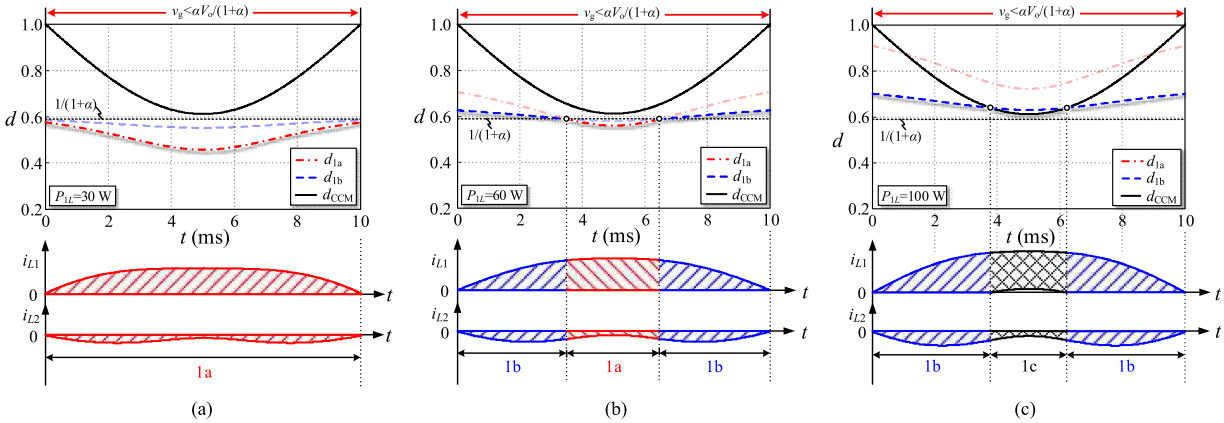

Fig. 16. Envelope of inductor current in a half line cycle at (a) $P_{1L} = 30$ W, (b) $P_{1L} = 60$ W, and (c) $P_{1L} = 100$ W, when $V_{\text{in}} = 110$ V and $\alpha = 0.7$.

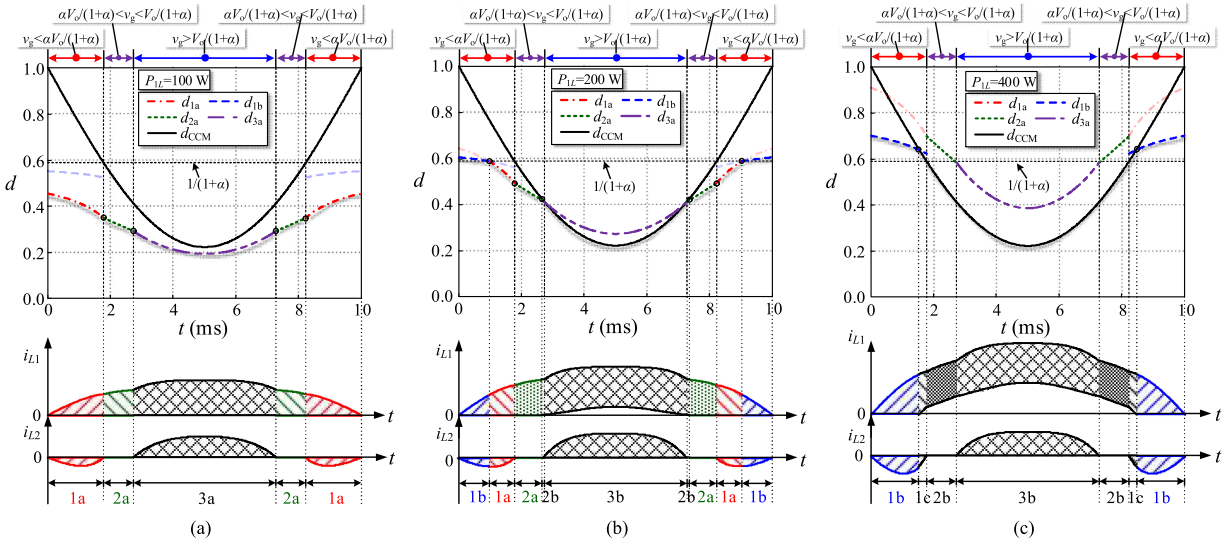

Fig. 17. Envelope of inductor current in a half line cycle at (a) $P_1L = 100$ W, (b) $P_{1L} = 200$ W, and (c) $P_{1L} = 400$ W, when $V_{\text{in}} = 220$ V and $\alpha = 0.7$.

When V_{in} and P_{1L} are fixed, the operation modes and the winding current waveforms in a half line cycle are fixed. On the basis of Figs. 3–5, the average inductor current of non-operation phase i_{L2_avg} can be calculated as (25) shown at the bottom of this page, and

$$P_{2L} = 2f_{\text{line}} \cdot \sum_{i=1}^{n} \int_{t_{i\_\min}}^{t_{i\_\max}} v_g i_{L2\_\text{avg}\_i} dt \tag{26}$$

where n is the number of operation modes in a half line cycle, $t_{i\_\min}$ and $t_{i\_\max}$ the start and end time of the ith operation mode,

$$i_{L2\_\text{avg}} = \begin{cases} \alpha P_{1L} v_g \left[\alpha V_o - (1+\alpha) v_g\right] / \left\{V_{\text{in}}^2 \left[\alpha(1+\alpha) v_g - V_o\right]\right\} & \text{Mode 1a} \\ \dfrac{\alpha v_g \left[2V_{\text{in}} \sqrt{2L_{cp} P_{1L} f_s V_o (1-\alpha)(1+\alpha)^2 \left[V_o - (1+\alpha) v_g\right] + \alpha V_{\text{in}}^2 \left[V_o^2 - (1+\alpha)^2 V_o v_g + \alpha(1+\alpha)^2 v_g^2\right]} \right.}{\left. +(1+\alpha) V_{\text{in}}^2 (2\alpha v_g - V_o) - 2L_{cp} P_{1L} f_s V_o (1-\alpha^2)\right]} & \text{Mode 1b} \\ \qquad\qquad 2L_{cp} V_o V_{in}^2 f_s (\alpha^2 - 1) & \\ \alpha v_g \left[(1+\alpha) v_g - \alpha V_o\right] / \left[2 f_s L_{cp} V_o (1-\alpha)(1+\alpha)^2\right] & \text{Mode 1c} \\ 0 & \text{Modes 2a, 2b} \\ 2P_{1L} \alpha v_g \left[(1+\alpha) v_g - V_o\right] / \left\{V_{\text{in}}^2 \left[(1+\alpha) v_g - \alpha^2 V_o\right]\right\} & \text{Mode 3a} \\ \alpha (V_o - v_g) \left[(1+\alpha) v_g - V_o\right] / \left[2 L_{cp} f_s V_o (1+\alpha)(1-\alpha^2)\right] & \text{Mode 3b} \end{cases} \tag{25}$$

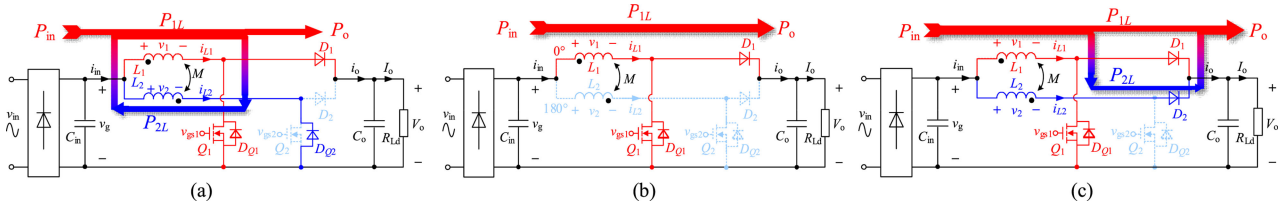

Fig. 18. Power distribution of each phase when (a) $v_g < \alpha V_o/(1+\alpha)$, (b) $\alpha V_o/(1+\alpha) \le v_g \le V_o/(1+\alpha)$, and (c) $v_g > V_o/(1+\alpha)$.

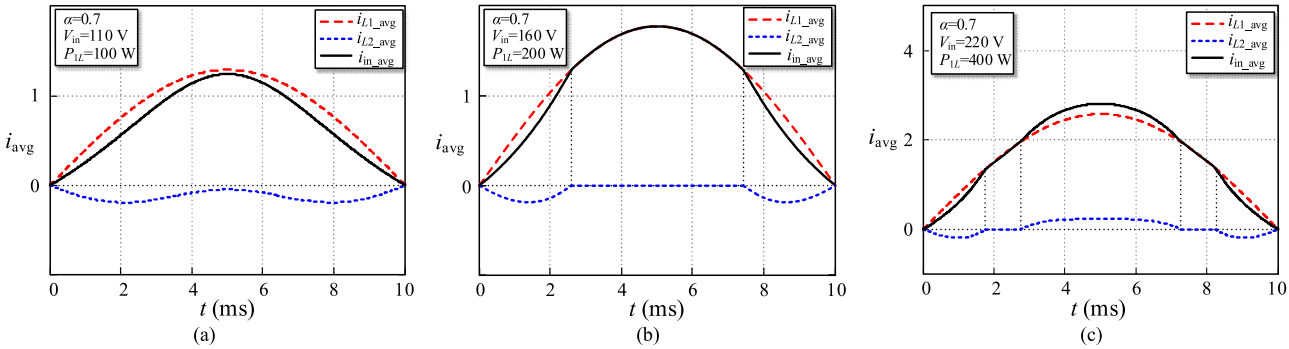

Fig. 19. Waveforms of average current in a half line cycle when (a) $V_{\rm in} = 110$ V, (b) $V_{\rm in} = 160$ V, and (c) $V_{\rm in} = 220$ V.

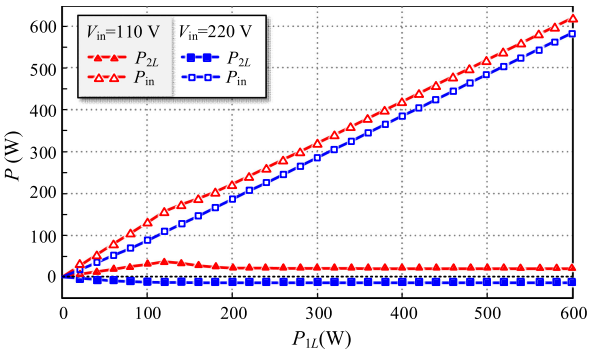

Fig. 20. Calculated power distribution between the two phases.

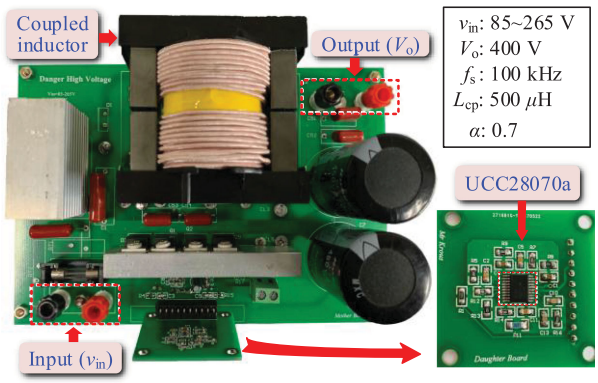

Fig. 21. Prototype of the two-phase interleaved boost PFC converter.

and $i_{L2\_avg\_i}$ the average inductor current of the ith operation mode of the non-operation phase.

Under the specifications listed in Section V, the average input and winding currents in a half line cycle, for $V_{\rm in}$ equals 110 and 220 V, can be obtained from (13) and (25), as shown in Fig. 19. Although i_{L1} is controlled in sinusoid, the average input current $i_{\rm in}$ is distorted because of the current flowing, i_{L2}, and the power factor will be decreased.

For a given P_{1L}, P_{2L} can be calculated from (26), and $P_{\rm in} = P_{1L} + P_{2L}$. Fig. 20 shows P_{2L} and $P_{\rm in}$ varying with P_{1L} at different $V_{\rm in}$ for $\alpha = 0.7$. When $V_{\rm in} = 110$ V, $\sqrt{2}V_{\rm in} < \alpha V_o/(1+\alpha)$; i_{L2} keeps negative in a half line cycle, so $P_{2L} < 0$ and the power flows through the non-operation phase returning back to the source. When $V_{\rm in} = 220$ V, $\sqrt{2}V_{\rm in} > V_o/(1+\alpha)$, although the three power distribution types in Fig. 18 exist in a half line cycle, the returned back power is limited because of the narrow time range and the overall power of the non-operation phase, $P_{2L} > 0$.

V. Experimental Verification

A 1-kW two-phase interleaved boost PFC converter is built for experimental verification, as shown in Fig. 21. $V_o = 400$ V, $f_s = 100$ kHz, $L_{cp} = 500\,\mu$H (ferrite ETD 59), and $\alpha = 0.7$, and the control IC is TI UCC28070a.

For $V_{\rm in} = 110$ V, $\sqrt{2}V_{\rm in} < \alpha V_o/(1+\alpha)$, Modes 1a, 1b, and 1c may appear in a half line cycle, and $P_{11} = 42$ W, $P_{12} = 66$ W, $P_{13} = 84$ W, and $P_{14} = 306$ W. Figs. 22(a), 23(a), and 24(a) show the experimental waveforms of the two inductor currents in a half line cycle when $P_{1L} = 30$ W, $P_{1L} = 60$ W, and $P_{1L} = 100$ W, respectively.

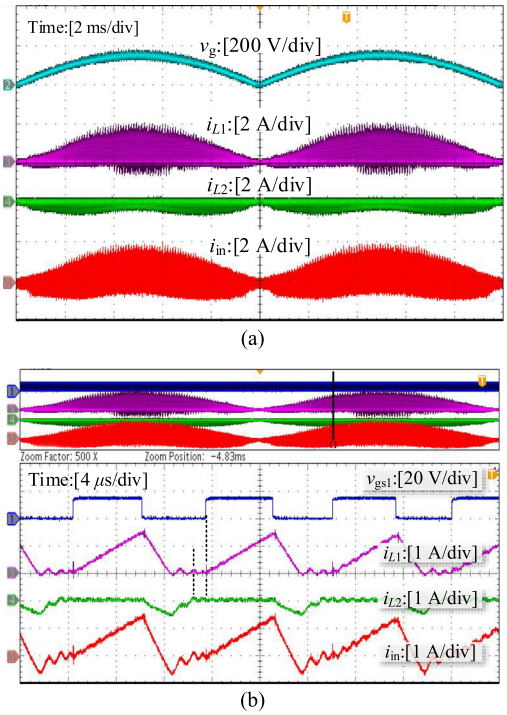

Fig. 22. Experimental waveforms of inductor current in (a) a half line cycle and (b) Mode 1a, when $V_{\text{in}} = 110$ V and $P_{1L} = 30$ W.

1) When $P_{1L} = 30$ W, $P_{2L} = -4$ W and $P_{\text{in}} = 26$ W. For $P_{1L} < P_{11}$, only Mode 1a occurs in [0, $T_{\text{line}}/2$], and the experimental waveforms of Mode 1a in the switching cycle are shown in Fig. 22(b). i_{L2} decreases to 0 in the negative direction before the next switching cycle, which matches the waveforms of Mode 1a in Fig. 3(a).
2) When $P_{1L} = 60$ W, $P_{2L} = -8$ W and $P_{\text{in}} = 52$ W. For $P_{11} < P_{1L} < P_{12}$, Modes 1b and 1a occur successively, and the experimental waveforms of Modes 1b and 1a in the switching cycle are shown in Fig. 23(b) and (c). In Fig. 23(b), i_{L2} does not reach 0 before the next switching cycle, which matches the waveforms of Mode 1b in Fig. 3(b).
3) When $P_{1L} = 100$ W, $P_{2L} = -12$ W and $P_{\text{in}} = 88$ W. For $P_{13} < P_{1L} < P_{14}$, Modes 1b and 1c occur in [0, $T_{\text{line}}/2$], and the experimental waveforms of Modes 1b and 1c in the switching cycle are shown in Fig. 24(b) and (c). In Fig. 24(c), i_{L1} does not reach 0 before the next switching cycle, which matches the waveforms of Mode 1c in Fig. 3(c).

The modes occurring in a half line cycle at different P_{1L} match the theoretical analysis in Figs. 12, 13, and 16.

For $V_{\text{in}} = 220$ V, $\sqrt{2}V_{\text{in}} > V_o/(1+\alpha)$, all the modes exist in a half line cycle, and $P_{32} = 167$ W, $P_{33} = 199$ W, $P_{34} = 285$ W, and $P_{35} = 1223$ W. Figs. 25(a), 26(a), and 27(a) show the experimental waveforms of the two inductor currents in a half line cycle when $P_{1L} = 100$ W, $P_{1L} = 200$ W, and $P_{1L} = 400$ W, respectively.

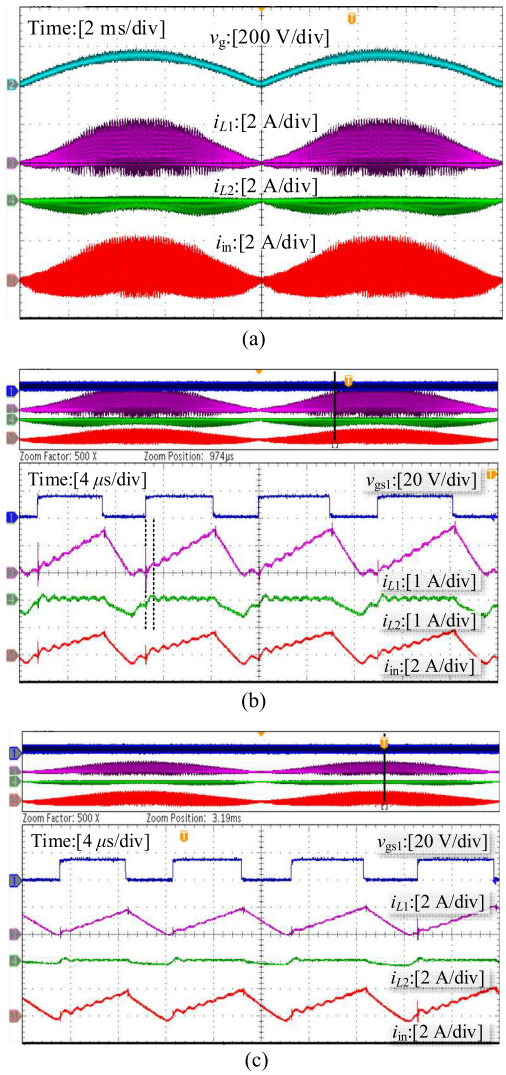

Fig. 23. Experimental waveforms of inductor current in (a) a half line cycle, (b) Mode 1b, and (c) Mode 1a, when $V_{\text{in}} = 110$ V and $P_{1L} = 60$ W.

1) When $P_{1L} = 100$ W, $P_{2L} = 30$ W, and $P_{\text{in}} = 130$ W: For $P_{1L} < P_{31}$, Modes 1a, 2a, and 3a occur, and the experimental waveforms of these modes in the switching cycle are shown in Fig. 25(b)–(d). In Fig. 25(c), i_{L1} is discontinuous and i_{L2} remains 0 in the switching cycle, which matches the waveforms of Mode 2a in Fig. 4(a). In Fig. 25(d), i_{L1} is discontinuous and i_{L2} remains positive in the switching cycle, which matches the waveforms of Mode 3a in Fig. 5(a).
2) When $P_{1L} = 200$ W, $P_{2L} = 20$ W, and $P_{\text{in}} = 220$ W: For $P_{33} < P_{1L} < P_{34}$, Modes 1b, 1a, 2a, 2b, and 3b occur in [0, $T_{\text{line}}/2$] successively, and the experimental waveforms of these modes in the switching cycle are shown in Fig. 26(b)–(e). Because of the control strategy of UCC28070a, which fixes the duty cycle below 0.5 at the zero-crossing point of the input voltage, Mode 1b does not appear in the experiment. In Fig. 26(d), i_{L1} is continuous

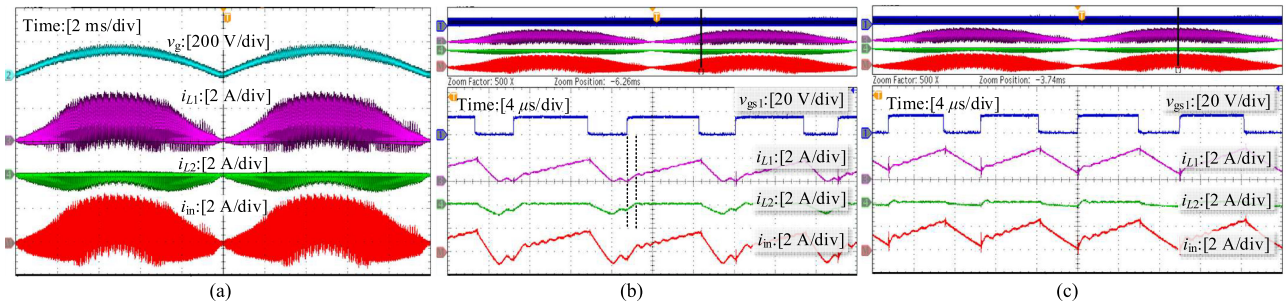

Fig. 24. Experimental waveforms of inductor current in (a) a half line cycle, (b) Mode 1b, and (c) Mode 1c, when $V_{\text{in}} = 110$ V and $P_{1L} = 100$ W.

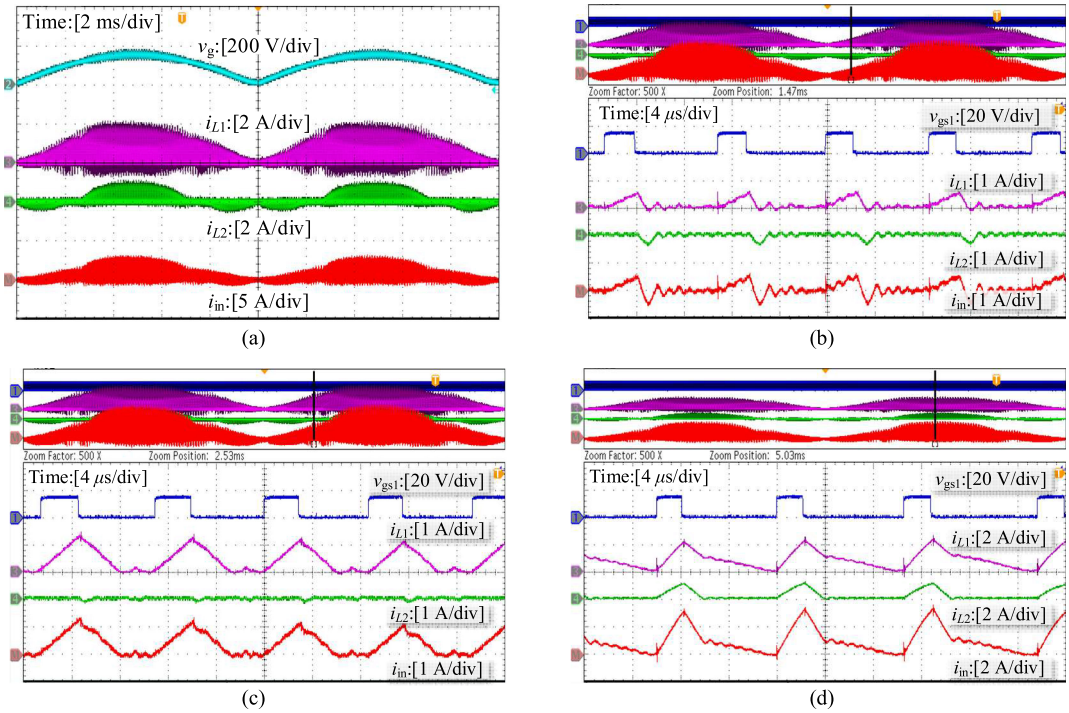

Fig. 25. Experimental waveforms of inductor current in (a) a half line cycle, (b) Mode 1a, (c) Mode 2a, and (d) Mode 3a, when $V_{\text{in}} = 220$ V and $P_{1L} = 100$ W.

and i_{L2} remains 0 in the switching cycle, which matches the waveforms of Mode 2b in Fig. 4(b). In Fig. 26(e), i_{L1} is continuous and i_{L2} remains positive, which matches the waveforms of Mode 3b in Fig. 5(b).

3) When $P_{1L} = 400$ W, $P_{2L} = 20$ W, and $P_{\text{in}} = 420$ W: For $P_{1L} > P_{34}$, Modes 1b, 1c, 2b, and Mode 3b occur successively, and the experimental waveforms of these modes in the switching cycle are shown in Fig. 27(b)–(e).

Generally, the modes in a half line cycle at different P_{1L} match the theoretical analysis in Figs. 14, 15, and 17.

The powers of the two phases are measured by using the PW3335 power meter, separately, and the experimental data of P_{2L} and P_{in} varying with P_{1L} in the experiment when $V_{\text{in}} = 110$ V and $V_{\text{in}} = 220$ V are shown in Fig. 28. The experimental results match the theoretical analysis under the low line condition for its simple operation modes, and a slight deviation (0–20 W) appears for the high line condition in a light load (<200 W). A possible reason would be that the operation modes in real experiments do not match those in the theoretical analysis. Since the duty cycle at the zero-crossing point of the input voltage is limited to below 50% by control IC UCC28070a, which is lower than the theoretical duty cycle values, the average input current and the input power of the non-operation phase are reduced in the experiments.

Fig. 29 shows the efficiency, η, of the converter with a coupled inductor varying with P_{in} under the single-phase and two-phase operations. When $V_{\text{in}} = 110$ V, $\sqrt{2}V_{\text{in}} < \alpha V_o/(1+\alpha)$. Since $P_{2L} < 0$, the losses of the converter increase, and the superiority of the single-phase operation in the light load is not obvious. The efficiency of the single-phase operation is close to that of the two-phase operation, and the efficiency change point is in a very light load, as shown in Fig. 31(a). When $V_{\text{in}} = 160$ V, $\alpha V_o/(1+\alpha) < \sqrt{2}V_{\text{in}} < V_o/(1+\alpha)$; the section of $P_{2L} = 0$ occurs, and the section of $P_{2L} < 0$ shrinks, so the superiority of the single-phase operation in the light load appears, as shown in Fig. 31(b). When $V_{\text{in}} = 220$ V, $\sqrt{2}V_{\text{in}} > V_o/(1+\alpha)$; the

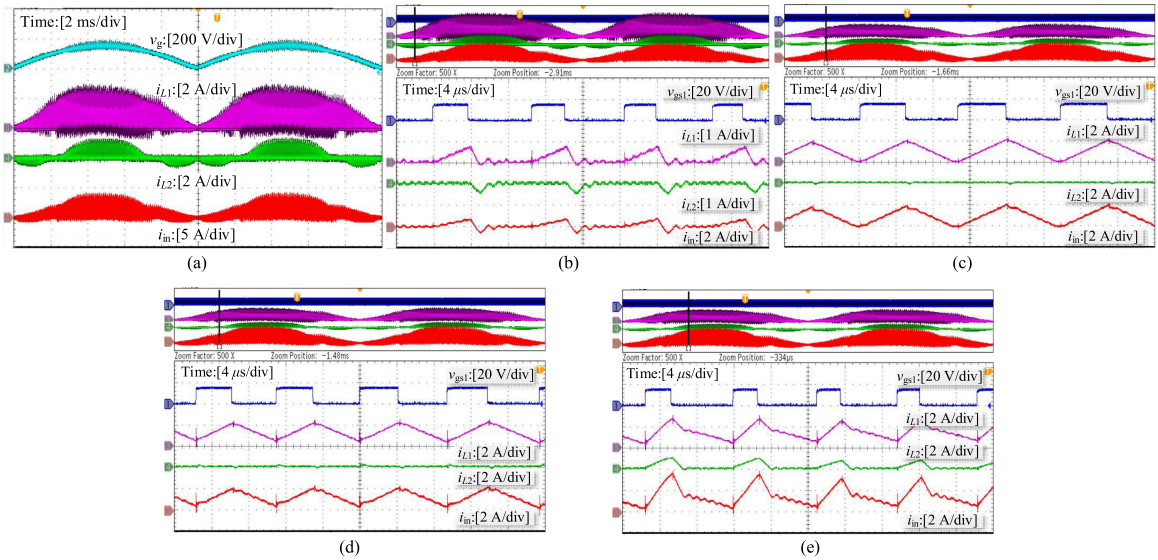

Fig. 26. Experimental waveforms of inductor current in (a) a half line cycle, (b) Mode 1a, (c) Mode 2a, (d) Mode 2b, and (e) Mode 3b, when $V_{\rm in} = 220$ V and $P_{1L} = 200$ W.

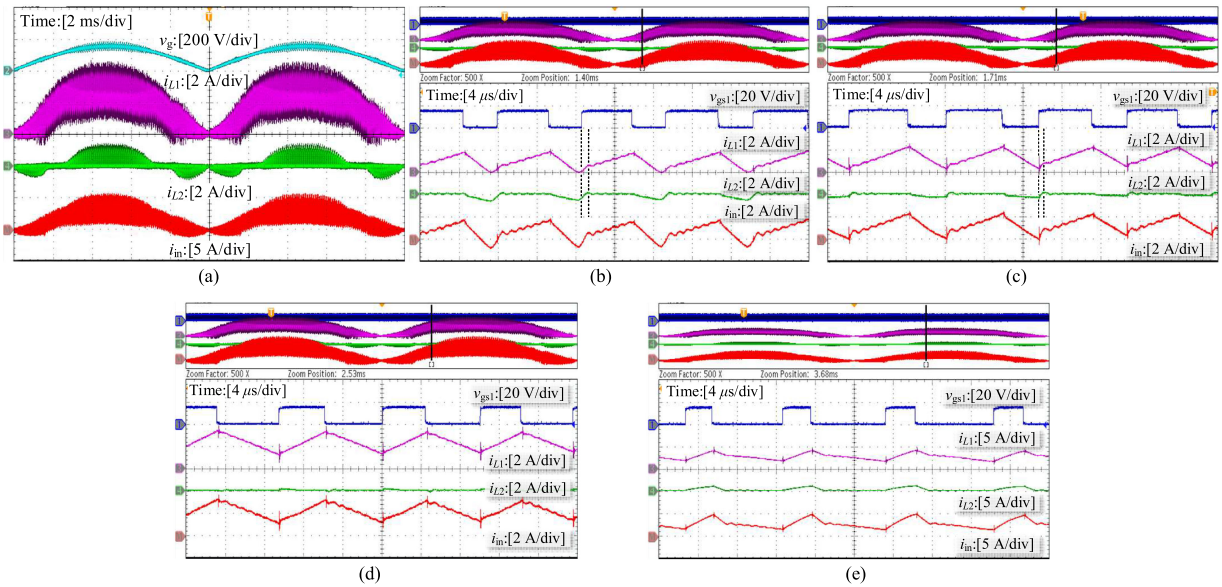

Fig. 27. Experimental waveforms of (a) a half line cycle, (b) Mode 1b, (c) Mode 1c, (d) Mode 2b, and (e) Mode 3b, when $V_{\rm in} = 220$ V and $P_{1L} = 400$ W.

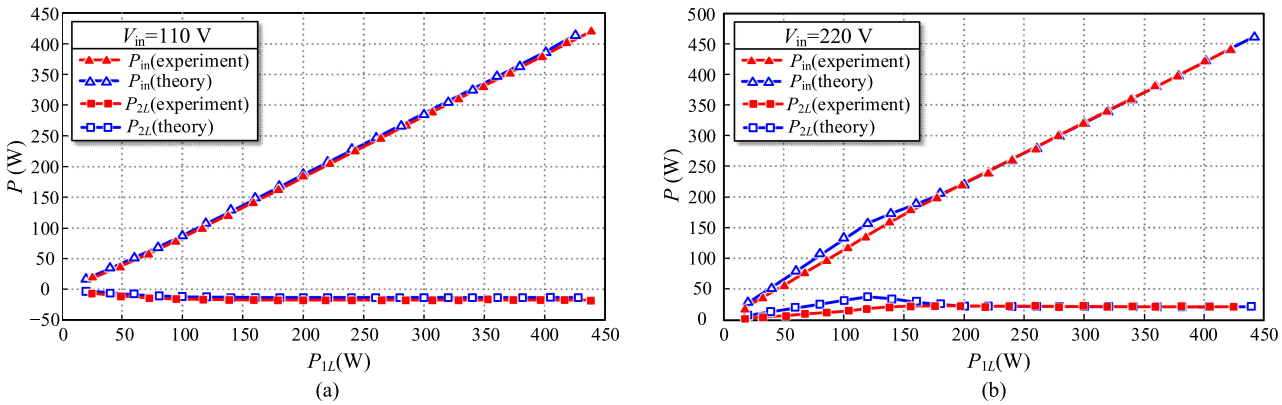

Fig. 28. Power comparison between experimental tests and theoretical calculation when (a) $V_{\rm in} = 110$ V and (b) $V_{\rm in} = 220$ V.

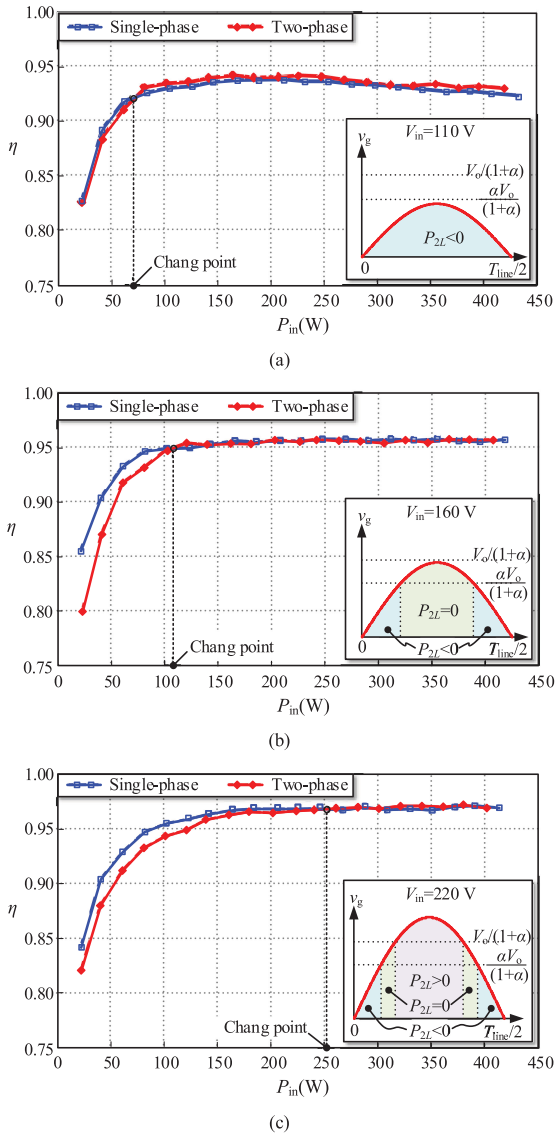

Fig. 29. Efficiency comparison between single-phase and two-phase operation converters with coupled inductor when (a) $V_{\rm in} = 110$ V, (b) $V_{\rm in} = 160$ V, and (c) $V_{\rm in} = 220$ V.

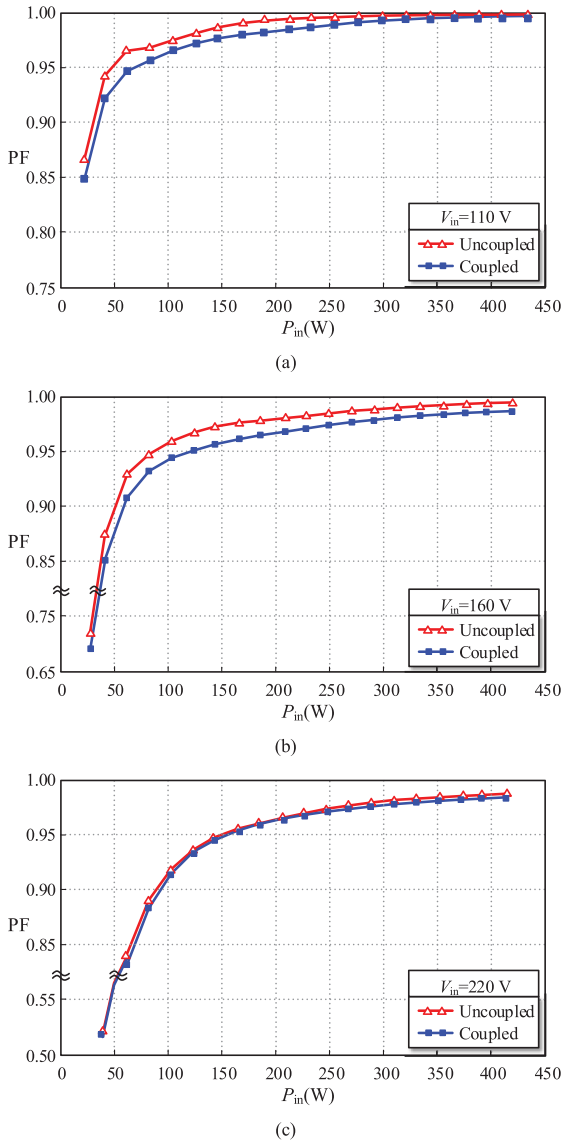

Fig. 30. PF comparison between single-phase operation converter with coupled inductor and uncoupled inductor, when (a) $V_{\rm in} = 110$ V, (b) $V_{\rm in} = 160$ V, and (c) $V_{\rm in} = 220$ V.

section of $P_{2L} < 0$ is further reduced, and the superiority of the single-phase operation in the light load is obvious, as shown in Fig. 31(c).

Fig. 30 shows the converter PF varying with $P_{\rm in}$ under the single-phase operation condition for the coupled inductor and uncoupled inductor cases. Because of the current flowing through the non-operation phase, the PF of the converter with a coupled inductor is generally lower than that of the uncoupled case in the whole load range. For a fixed input voltage, as the load increases, the proportion of P_{2L} in $P_{\rm in}$ becomes small, and the influence of i_{L2} on $i_{\rm in}$ is reduced. Therefore, the PF of the single-phase converter with a coupled inductor and an uncoupled inductor is close at the heavy load. For a fixed load, with the increase of $V_{\rm in}$, the section of $P_{2L} < 0$ and the average current of i_{L2} are reduced, so the influence of the non-operation phase on the PF becomes small, and the PFs of the coupled and uncoupled cases are close.

VI. Conclusion

In this paper, the operation modes of the two-phase interleaved boost PFC converter with a coupled inductor under the single-phase operation are analyzed in detail. All the seven operation modes and their boundary conditions in a switching cycle are presented. Then, the operation modes in a half line cycle, as well as their load-related variation rules, are obtained, which can be used to predict the converter operation mode under any condition. Since negative current flows through the non-operation phase caused by the coupled inductor, the converter efficiency and PF will be reduced, especially under low line voltage. The coupling effect is relatively weak under a high line voltage due to the low average winding current and the narrow time range of the negative power flow, inside which the superiority of the single-phase operation is obvious.

REFERENCES

[1] H. Wei and I. Batarseh, "Comparison of basic converter topologies for power factor correction," in *Proc. IEEE Southeastcon '98*, 1998, pp. 348–353.

[2] B. A. Miwa, D. M. Otten, and M. E. Schlecht, "High efficiency power factor correction using interleaving techniques," in *Proc. IEEE Appl. Power Electron. Conf. Expo.*, 1992, pp. 557–568.

[3] L. Balogh and R. Redl, "Power-factor correction with interleaved boost converters in continuous-inductor-current mode," in *Proc. IEEE Appl. Power Electron. Conf. Expo.*, 1993, pp. 168–174.

[4] W. Martinez, S. Kimura, J. Imaoka, M. Yamamoto, and C. A. Cortes, "Volume comparison of DC-DC converters for electric vehicles," in *Proc. IEEE Workshop Power Electron. Power Qual. Appl.*, 2015, pp. 1–6.

[5] M. Pavlovský, G. Guidi, and A. Kawamura, "Assessment of coupled and independent phase designs of interleaved multiphase buck/boost DC–DC converter for EV power train," *IEEE Trans. Power Electron.*, vol. 29, no. 6, pp. 2693–2704, Jun. 2014.

[6] M. Hirakawa, M. Nagano, Y. Watanabe, K. Andoh, S. Nakatomi, and S. Hashino, "High power density DC/DC converter using the close-coupled inductors," in *Proc. IEEE Energy Convers. Congr. Expo.*, 2009, pp. 1760–1767.

[7] S. Chandrasekaran and L. U. Gokdere, "Integrated magnetics for interleaved DC-DC boost converter for fuel cell powered vehicles," in *Proc. IEEE 35th Annu. Power Electron. Spec. Conf.*, 2004, vol. 1, pp. 356–361.

[8] S. Kimura, J. Imaoka, and M. Yamamoto, "Downsizing effects of integrated magnetic components in high power density DC-DC converters for EV and HEV," in *Proc. IEEE Energy Convers. Congr. Expo.*, 2014, pp. 5761–5768.

[9] Y. Fang and X. Ma, "A novel PV microinverter with coupled inductors and double-boost topology," *IEEE Trans. Power Electron.*, vol. 25, no. 12, pp. 3139–3147, Dec. 2010.

[10] K. J. Hartnett, J. G. Hayes, M. S. Rylko, B. J. Barry, and J. W. Masłoń, "Comparison of 8-kW CCTT IM and discrete inductor interleaved boost converter for renewable energy applications," *IEEE Trans. Ind. Appl.*, vol. 51, no. 3, pp. 2455–2469, May/Jun. 2015.

[11] J. Li, C. R. Sullivan, and A. Schultz, "Coupled-inductor design optimization for fast-response low-voltage DC-DC converters," in *Proc. IEEE Appl. Power Electron. Conf. Expo.*, 2002, vol. 2, pp. 817–823.

[12] P. Zumel, O. Garcia, J. A. Cobos, and J. Uceda, "Magnetic integration for interleaved converters," in *Proc. IEEE Appl. Power Electron. Conf. Expo.*, 2003, vol. 2, pp. 1143–1149.

[13] H. Kosai, S. McNeal, B. Jordan, J. Scofield, B. Ray, and Z. Turgut, "Coupled inductor characterization for a high performance interleaved boost converter," *IEEE Trans. Magne.*, vol. 45, no. 10, pp. 4812–4815, Oct. 2009.

[14] J. Imaoka *et al.*, "A magnetic design method considering DC-biased magnetization for integrated magnetic components used in multi-phase boost converters," *IEEE Trans. Power Electron.*, vol. 33, no. 4, pp. 3346–3362, Apr. 2018.

[15] J. Imaoka, Y. Ishikura, T. Kawashima, and M. Yamamoto, "Optimal design method for interleaved single-phase PFC converter with coupled inductor," in *Proc. IEEE Energy Convers. Congr. Expo.*, 2011, pp. 1807–1812.

[16] H. Choi and L. Balogh, "A cross-coupled master–slave interleaving method for boundary conduction mode (BCM) PFC converters," *IEEE Trans. Power Electron.*, vol. 27, no. 10, pp. 4202–4211, Oct. 2012.

[17] D. O. Boillat and J. W. Kolar, "Modeling and experimental analysis of a coupling inductor employed in a high performance AC power source," in *Proc. Int. Conf. Renewable Energy Res. Appl.*, 2012, pp. 1–18.

[18] M. S. Ortmann, S. A. Mussa, and M. L. Heldwein, "Generalized analysis of a multistate switching cells-based single-phase multilevel PFC rectifier," *IEEE Trans. Power Electron.*, vol. 27, no. 1, pp. 46–56, Jan. 2012.

[19] K. Martín, A. Rujas, I. Villar, I. Perez-de-Arenaza, and I. Etxeberria-Otadui, "Design of a 2.5 kW PFC boost full-SiC converter based on close-coupled inductors," in *Proc. IEEE 15th Workshop Control Model. Power Electron.*, 2014, pp. 1–7.

[20] Y. Itoh, F. Hattori, S. Kimura, J. Imaoka, and M. Yamamoto, "Design method considering magnetic saturation issue of coupled inductor in interleaved CCM boost PFC converter," in *Proc. IEEE Energy Convers. Congr. Expo.*, 2015, pp. 2616–2621.

[21] P. Zumel, C. Fernández, A. de Castro, and O. García, "Efficiency improvement in multiphase converter by changing dynamically the number of phases," in *Proc. IEEE Power Electron. Spec. Conf.*, 2006, pp. 1–6.

[22] W. Qiu, C. Cheung, S. Xiao, and G. Miller, "Power loss analyses for dynamic phase number control in multiphase voltage regulators," in *Proc. IEEE Appl. Power Electron. Conf.. Expo.*, 2009, pp. 102–108.

[23] J. Su and C. Liu, "A novel phase-shedding control scheme for improved light load efficiency of multiphase interleaved DC–DC converters," *IEEE Trans. Power Electron.*, vol. 28, no. 10, pp. 4742–4752, Oct. 2013.

[24] C. Wang, M. Xu, F. C. Lee, and Z. Luo, "Light load efficiency improvement for multi-channel PFC," in *Proc. IEEE Power Electron. Spec. Conf.*, 2008, pp. 4080–4085.

[25] Y. C. Chen, J. D. Hsu, Y. A. Ang, and T. Y. Yang, "A new phase shedding scheme for improved transient behavior of interleaved boost PFC converters," in *Proc. IEEE Appl. Power Electron. Conf.. Expo.*, 2014, pp. 1916–1919.

[26] J. Imaoka *et al.*, "Magnetic design and experimental evaluation of integrated magnetic components used in interleaved multi-phase DC/DC converter with phase drive control," in *Proc. IEEE 3rd Int. Future Energy Electron. Conf. ECCE Asia*, 2017, pp. 2192–2197.

[27] B. C. Barry, J. G. Hayes, and M. S. Ryłko, "CCM and DCM operation of the interleaved two-phase boost converter with discrete and coupled Inductors," *IEEE Trans. Power Electron.*, vol. 30, no. 12, pp. 6551–6567, Dec. 2015.

[28] F. Yang, X. Ruan, G. Wu, and Z. Ye, "Discontinuous-current mode operation of a two-phase interleaved boost DC–DC converter with coupled inductor," *IEEE Trans. Power Electron.*, vol. 33, no. 1, pp. 188–198, Jan. 2018.

[29] F. Yang, X. Ruan, Y. Yang, and Z. Ye, "Interleaved critical current mode boost PFC converter with coupled inductor," *IEEE Trans. Power Electron.*, vol. 26, no. 9, pp. 2404–2413, Sep. 2011.

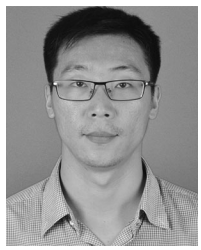

Fei Yang (M'16) was born in Shanxi, China, in 1983. He received the B.S. and Ph.D. degrees in electrical engineering from the Nanjing University of Aeronautics and Astronautics, Nanjing, China, in 2006 and 2013, respectively.

From February 2014 to October 2015, he was a Postdoctoral Research Fellow with the Department of Mechanical Engineering, KU Leuven, Leuven, Belgium. In 2015, he joined the Faculty of Electrical Engineering Teaching and Research Division, School of Automation, Nanjing University of Science and Technology, Nanjing, China, and he was engaged in teaching and research in the field of power electronics. His main research interests include PFC converters, EMI filter design, and pulse power generator for electrical discharge machine.

Chunhui Li was born in Jiangsu Province, China, in 1990. He received the B.S. degree in electrical engineering and automation from Nantong University, Nantong, China, in 2013, and the M.S. degree in power electronics from Nanjing University of Science and Technology, Nanjing, China, in 2019.

His main research interest focuses on power-factor correction.

Yong Cao was born in Anhui Province, China, in 1992. He received the B.S. degree in electrical engineering and automation from Liaoning Technical University, Fuxin, China, in 2016, and the M.S. degree in electrical engineering from Nanjing University of Science and Technology, Nanjing, China, in 2019.

His main research interest focuses on electromagnetic interface prediction and EMI filter design.

Kai Yao (M'14) was born in Jiangsu Province, China, in 1980. He received the B.S. degree in industrial automation from Nantong University, Nantong, China, in 2002, the M.S. degree in mechanical design and theory, in 2005, and the Ph.D. degree in electrical engineering from Nanjing University of Aeronautics and Astronautics, Nanjing, China, in 2010.

In 2011, he joined the Faculty of Electrical Engineering, School of Automation, Nanjing University of Science and Technology, Nanjing, China, where he has been engaged in teaching and research in the field of power electronics. His main research interests include power-factor correction converters and condition monitoring and diagnostics of power converters.